







ARTICLE

Rac1 promotes kidney collecting duct integrity by limiting actomyosin activity

Fabian Bock¹ , Bertha C. Elias¹ , Xinyu Dong¹, Diptiben V. Parekh^{1,2}, Glenda Mernaugh¹, Olga M. Viquez¹, Anjana Hassan¹, Venkateswara Rao Amara¹ , Jiageng Liu¹ , Kyle L. Brown¹, Andrew S. Terker¹, Manuel Chiusa^{1,3}, Leslie S. Gewin^{1,3,6}, Agnes B. Fogo⁴, Cord H. Brakebusch⁵, Ambra Pozzi^{1,3,7} , and Roy Zent^{1,3,6} 

A polarized collecting duct (CD), formed from the branching ureteric bud (UB), is a prerequisite for an intact kidney. The small Rho GTPase Rac1 is critical for actin cytoskeletal regulation. We investigated the role of Rac1 in the kidney collecting system by selectively deleting it in mice at the initiation of UB development. The mice exhibited only a mild developmental phenotype; however, with aging, the CD developed a disruption of epithelial integrity and function. Despite intact integrin signaling, Rac1-null CD cells had profound adhesion and polarity abnormalities that were independent of the major downstream Rac1 effector, Pak1. These cells did however have a defect in the WAVE2–Arp2/3 actin nucleation and polymerization apparatus, resulting in actomyosin hyperactivity. The epithelial defects were reversible with direct myosin II inhibition. Furthermore, Rac1 controlled lateral membrane height and overall epithelial morphology by maintaining lateral F-actin and restricting actomyosin. Thus, Rac1 promotes CD epithelial integrity and morphology by restricting actomyosin via Arp2/3-dependent cytoskeletal branching.

Introduction

The renal collecting duct (CD) is a polarized epithelial monolayer that provides structure and protection and fine-tunes water and electrolyte homeostasis by the kidney. It does this by enabling tightly regulated directional flow of water and electrolytes via transporters and channels like aquaporin 2 (AQP2) and the epithelial sodium channel (Leiz and Schmidt-Ott, 2019). Disruption of the structural integrity of the CD results in pathological states such as nephrogenic diabetes insipidus (Pearce et al., 2015). The kidney CD system is formed from the ureteric bud (UB), which undergoes iterative rounds of branching morphogenesis, most of which occurs by embryonic day 17.5 (E17.5; Cebrián et al., 2004). This highly regulated process requires growth factor-dependent signaling and cell-ECM interaction (Costantini and Kopan, 2010). An intact actin cytoskeleton is a key requirement for renal epithelial cells to undergo development and maintain their integrity during normal homeostasis, as it orders cellular space, transduces force, and permits junction formation required for a polarized barrier (Denker and Sabath, 2011; Kumaran and Hanukoglu, 2020; Rodgers and Fanning, 2011).

The small Rho GTPase Rac1 is a molecular switch with multiple cell type- and context-dependent functions that coordinates actin cytoskeletal dynamics (Bosco et al., 2009). Integrin interactions with ECM trigger Rac1 activation, and Rac1 in turn induces effector proteins (Berrier et al., 2002). The best-characterized Rac1 effector protein, p21-activated kinase 1 (Pak1), regulates the phosphorylation status of the actin depolymerizing factor cofilin, thus controlling actin turnover (Delorme et al., 2007). Rac1 also activates the Wiskott-Aldrich syndrome protein family members such as WAVE2, which release their VCA (verprolin, central, and acidic) domain to bind to and activate the Arp2/3 complex (Chen et al., 2017). Arp2/3 nucleates (formation of new filaments from monomers) and polymerizes actin to create a branched actin network required for many cellular processes, including stable cellular protrusions and normal epithelial cell-cell junctions (Brieher and Yap, 2013; Goley and Welch, 2006). In addition to its role of regulating actin polymerization, Rac1 modulates actomyosin activity by mechanisms that are largely dependent on its crosstalk with RhoA,

¹Division of Nephrology and Hypertension, Department of Medicine, Vanderbilt University Medical Center, Nashville, TN; ²Department of Immunology and Microbiology, The Scripps Research Institute, La Jolla, CA; ³Department of Veterans Affairs Hospital, Nashville, TN; ⁴Department of Pathology, Microbiology and Immunology, Vanderbilt University Medical Center, Nashville, TN; ⁵Biotech Research Center, University of Copenhagen, Copenhagen, Denmark; ⁶Department of Cell and Developmental Biology, Vanderbilt University School of Medicine, Nashville, TN; ⁷Department of Molecular Physiology & Biophysics, Vanderbilt University School of Medicine, Nashville, TN.

Correspondence to Roy Zent: roy.zent@vumc.org.

© 2021 Bock et al. This article is distributed under the terms of an Attribution-Noncommercial-Share Alike-No Mirror Sites license for the first six months after the publication date (see <http://www.rupress.org/terms/>). After six months it is available under a Creative Commons License (Attribution-Noncommercial-Share Alike 4.0 International license, as described at <https://creativecommons.org/licenses/by-nc-sa/4.0/>).

another member of the small GTPase family (Chauhan et al., 2011; Daneshjou et al., 2015; Yu et al., 2008).

Branching morphogenesis is a key developmental process required for the formation of organs that consist of branched epithelial tubes (Goodwin and Nelson, 2020). There is overwhelming evidence using cell culture and organ explants that Rac1 plays a key role in epithelial tubulogenesis and branching of the lung and mammary gland (Danopoulos et al., 2016; Morrison et al., 2015; Tushir and D'Souza-Schorey, 2007; Zhu and Nelson, 2013). In addition, Rac1 is required for normal tube formation of the primitive *Drosophila* salivary gland and trachea. It has also been shown to be vital for normal branching and development of the vasculature in mice (Tan et al., 2008). There are, however, no data defining the role of Rac1 in epithelial cell branching morphogenesis in vivo in mammals. To gain insight into the role of Rac1 in the kidney collecting system, a major epithelial structure that forms by undergoing tubulogenesis and branching morphogenesis, we deleted it in the UB at E10.5, when the UB is formed. Contrary to expectations, the UB branching morphogenesis phenotype was mild; however, the mice developed progressive abnormalities in CD tubular structure, morphology, and function as they aged. We describe the cellular mechanisms underlying these pathological findings.

Results

Rac1 is required for normal CD development

To delineate the in vivo function of Rac1 in the developing CD, we deleted it specifically in the developing UB by crossing floxed Rac1 (Rac1^{fl/fl}) mice with Hoxb7-cre mice, which express Cre recombinase in the Wolffian duct and UB starting at E10.5. The Hoxb7:Rac1^{fl/fl} mice were born in the predicted Mendelian ratio, and they did not die prematurely due to a lethal kidney developmental phenotype despite successful Rac1 deletion as confirmed by immunoblotting of isolated papillae of 1-wk-old pups (Fig. 1 A). To determine if there was normal development of the collecting system, we examined kidneys at 1 and 6 mo of age. The 6-mo-old mutant kidneys were moderately smaller (Fig. 1 B). At 1 mo, Hoxb7:Rac1^{fl/fl} kidneys displayed mild branching morphogenesis defects characterized by smaller papillae with fewer tubules (Fig. 1 C). By 6 mo, there was advanced CD dilatation and a flattened epithelium, with cells growing on top of each other into the lumen, suggesting a polarity defect (Fig. 1 D). Furthermore, there was significant tubulointerstitial fibrosis (Fig. 1, D and E), as shown by picrosirius red staining (bottom panels). To define the kidney collecting system functional status, we assessed the urine-concentrating ability of the mice after 24 h of water deprivation. In contrast to the Rac1^{fl/fl} mice, the Hoxb7:Rac1^{fl/fl} mice were unable to maximally concentrate the urine and significantly decrease their urine output, resulting in more weight loss (Fig. 1, F–H). These data show that Rac1 does not play an essential role in UB formation. However, it is required for normal development, homeostasis, and function of the kidney collecting system.

The relatively mild branching morphogenesis phenotype of the Hoxb7:Rac1^{fl/fl} was surprising as Rac1 has been shown to play a critical role in epithelial cell polarization (Löf-Öhlin et al., 2017;

O'Brien et al., 2001; Yu et al., 2005). We therefore investigated when the phenotype first became evident and the mechanism underlying it. Kidneys from E13 and E15.5 Hoxb7:Rac1^{fl/fl} mice had no obvious developmental abnormalities when compared with Rac1^{fl/fl} controls (Fig. 2 A). However, a subtle branching defect was seen at E18.5 (fewer and more dilated papillary ducts) that worsened over time and became clearly visible in newborn mice (fewer and more dilated CDs; Fig. 2 A). This late mild branching phenotype suggested that Rac1 plays a role in regulating advanced stages of UB development. To determine whether this was due to temporal Rac1 expression, we investigated its expression levels during UB development. Rac1 is undetectable in the E15.5 UB of WT mice (Fig. 2 B) but readily detectable in newborns and enriched in adult mouse and human CDs (Fig. 2, C–E). A full spatiotemporal assessment of Rac1 protein levels in control CD tubular cross sections revealed that even at E17.5, there is minimal Rac1, but as mice age, Rac1 is increasingly expressed, and its localization progresses from basolateral to apical, suggesting differential functional specializations in polarized cells, consistent with previous data (Fig. S1; Couto et al., 2017; Yagi et al., 2012). Thus, Rac1 expression only occurs in late branching morphogenesis, which likely accounts for its relatively minor role in UB development.

Rac1 is required for normal CD polarization and differentiation

As Rac1 is only expressed late in CD development, we examined the role of this major actin cytoskeleton regulator on post-development CD polarity and differentiation. There was no difference in the E-cadherin expression pattern between newborn Hoxb7:Rac1^{fl/fl} and Rac1^{fl/fl} mice (Fig. 3 A), suggesting that Rac1 plays little role in maintaining CD polarity during development. However, there was a complete loss of junctional E-cadherin by 6 mo of age (Fig. 3 B), suggesting that Rac1 is required to maintain the epithelial phenotype of CDs as mice age. We further characterized the polarity defects in the Rac1-null CDs by staining for the apical membrane-actin cytoskeletal linker protein Ezrin and the primary cilia marker acetylated tubulin. Apical localization of Ezrin was lost, and although some cilia were present, there was a significant apical primary ciliary defect in 6-mo-old *Dolichus biflorus* agglutinin (DBA)-labeled CDs of Hoxb7:Rac1^{fl/fl} mice (Fig. 3, C and D). Furthermore, confocal immunofluorescence staining of AQP2 and single-cell apicobasal line-scan intensity profiling and quantification revealed that Rac1-null CDs had a marked defect in apical AQP2 localization (Fig. 3, E–G). These data suggest that Rac1 is required for CD epithelial apicobasal polarization and that there is mislocalization of AQP2 in Hoxb7:Rac1^{fl/fl} mice, which explains their urine-concentrating defect. Polarized deposition of a basement membrane is required for epithelial polarity (Morrisey and Sherwood, 2015). We next assessed the basement membrane of adult papillary inner medullary CDs of control and Hoxb7:Rac1^{fl/fl} mice by performing transmission EM (TEM; Fig. 3 H). This revealed that mutant basement membranes were severely abnormal with significant thinning (Fig. 3, H and I). It has been shown that during development Rac1 orients epithelial polarity via an autocrine pathway leading to basal laminin assembly (O'Brien et al., 2001; Yu et al., 2005). To test whether a similar mechanism applies to the CD

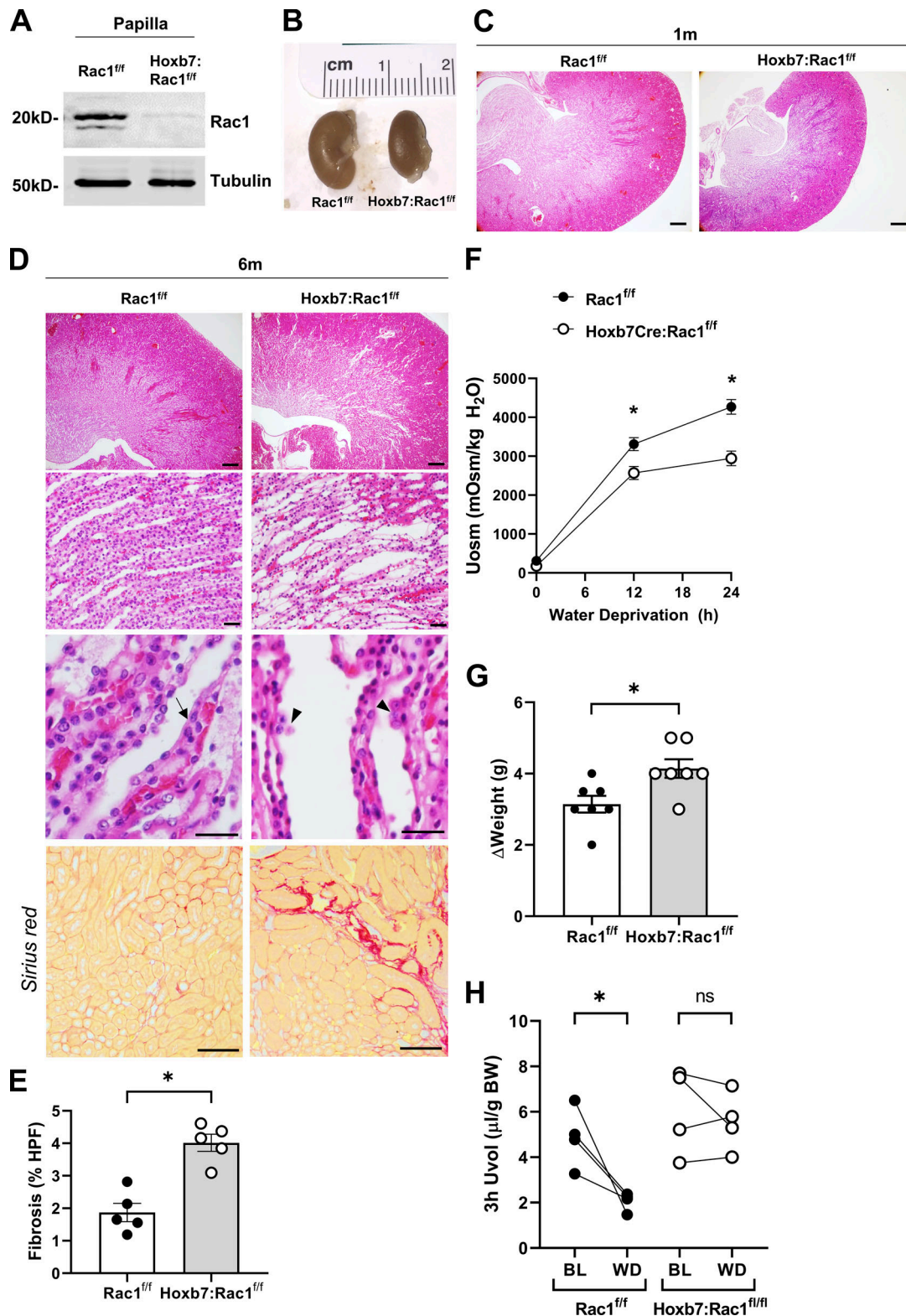


Figure 1. **Hoxb7:Rac1^{ff/ff} kidneys are small, have more fibrosis, and have a urine concentration defect.** (A) Rac1 expression in papillary lysates from 1-wk-old control mice (Rac1^{ff/ff}) and Hoxb7:Rac1^{ff/ff} mice was analyzed by immunoblotting. A representative immunoblot of four mice per group is shown. (B) Images of 6-mo-old Rac1^{ff/ff} and Hoxb7:Rac1^{ff/ff} kidneys. *n* = 5 mice per group. (C–E) Hematoxylin and eosin–stained paraffin kidney sections from 1-mo-old (C) and 6-mo-old (D) mice. Arrow in D (third row) indicates normal medullary epithelium, and arrowheads indicate epithelial cells growing on top of each other in the CD. *n* = 5 mice per group. Sirius red staining of 6-mo-old Hoxb7:Rac1^{ff/ff} and Rac1^{ff/ff} mice is shown in the bottom row. Five high-power fields per sample of red stained area in kidney cortex were quantified using ImageJ (E). Data were expressed as mean ± SEM. *n* = 5 mice per group. (F–H) Urine osmolality (F), body weight loss shown in Δweight (G), and 3-h urine volumes (H) are shown in Rac1^{ff/ff} and Hoxb7:Rac1^{ff/ff} mice following 24-h water deprivation. Data are expressed as mean ± SEM, *n* = 6–7 mice (F and G) or 4 mice (H) per group. Scale bars represent 200 μm (C), 100 μm (D, top row), 50 μm (D, second and third rows), and 100 μm (D, bottom row). *, *P* < 0.05.

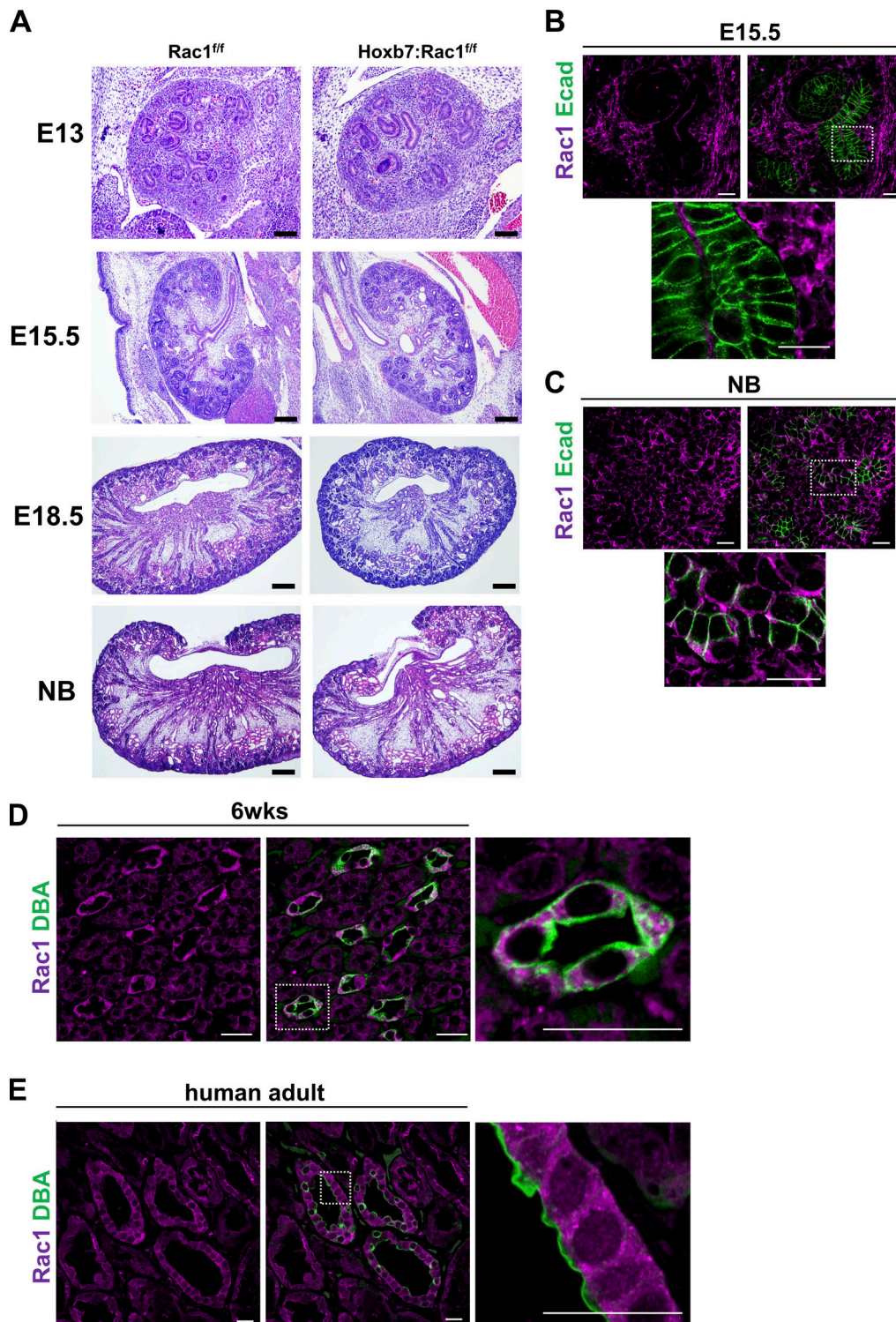


Figure 2. **Hoxb7:Rac1^{ff} kidneys have a mild developmental defect due to late Rac1 expression.** (A) Hematoxylin and eosin–stained kidneys of Rac1^{ff} and Hoxb7:Rac1^{ff} mice at different stages of development (NB, newborn). Note that there are fewer and more dilated CDs starting at E18.5. *n* = 5 mice per group. (B and C) Rac1 immunostaining (magenta, single channel on the left) was performed on WT paraffin kidney sections and the UB labeled with E-cadherin (Ecad; green, merged with Rac1 in red on the right) at E15.5 (B) and at birth (NB; C), with a focused area highlighted by a white dashed box. *n* = 3 mice per group. (D and E) Rac1 (magenta) was evident in 6-wk-old WT mice (D) and human healthy adult (E) CDs labeled with FITC-conjugated DBA (green). *n* = 3 mice or 2 human samples per group. Scale bars represent 100 μm (A) and 20 μm (B–E).

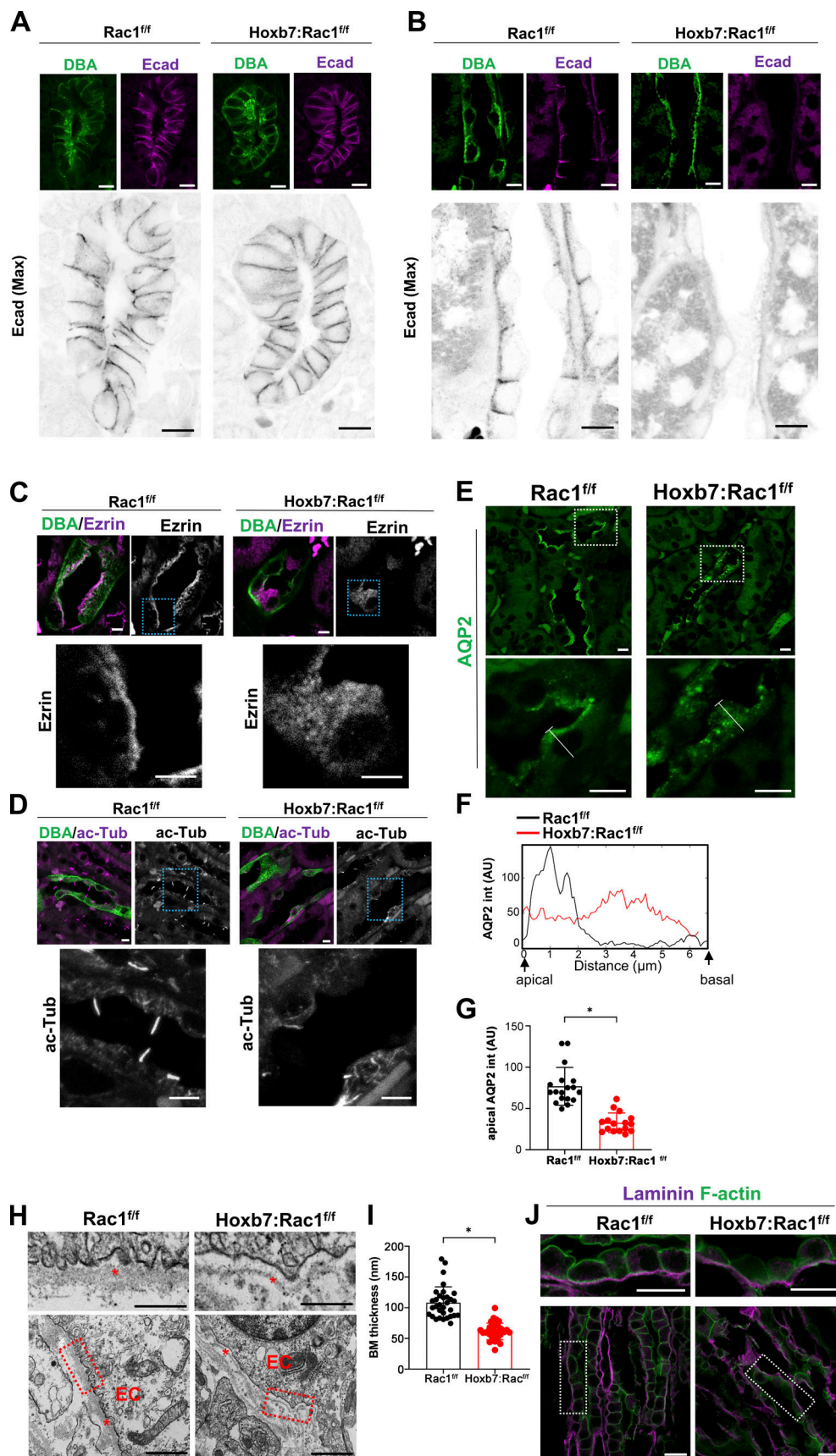


Figure 3. **Adult Hoxb7:Rac1^{fl/fl} CD cells have a polarization and differentiation defect.** (A and B) The CD cells of newborn (A) and 6-month-old adult (B) mice indicated were labeled with DBA (green) and stained for E-cadherin (Ecad, magenta) and imaged with confocal laser scanning microscopy. The bottom black and white

panels are full-thickness maximum intensity projections of at least five z-stacks. **(C)** $Rac1^{f/f}$ and $Hoxb7:Rac1^{f/f}$ adult (4 mo) CDs (marked by DBA, green) were immunostained for Ezrin (magenta) and analyzed by confocal microscopy. $n = 4$ mice per group. **(D)** CDs (marked by DBA, green) from 4-mo-old control and $Hoxb7:Rac1^{f/f}$ mice were immunostained for acetylated tubulin (ac-Tub; magenta). Shown (C, D) are full-thickness maximum intensity projections of a minimum of five z-stacks. $n = 3$ mice per group. **(E–G)** Kidney sections of 4-mo-old mice were immunostained for the CD-specific water channel AQP2 (green; E). $n = 3$ mice per group. A representative apicobasal single-cell line-scan profile (as indicated by the dashed white line in the image in E) is shown in F. Quantification of apical AQP2 intensity using ImageJ of at least 15 CDs from 3 mice is shown in G. Values represent mean \pm SD. **(H–J)** TEM was performed on inner medullary basement membranes (marked by a red asterisks; EC, epithelial cell) in the renal papilla of adult (10-mo-old) $Rac1^{f/f}$ and $Hoxb7:Rac1^{f/f}$ mice (H), and the thickness (in nanometers) was quantified at three randomly selected places per image (I). A minimum of 30 measurements per group is shown as mean \pm SD (I). Renal papillae of adult (10-mo-old) $Rac1^{f/f}$ and $Hoxb7:Rac1^{f/f}$ mice were immunostained for laminin ($\alpha 1$ subunit, magenta), colabeled with phalloidin (green), and analyzed by confocal microscopy (J). $n = 3$ mice/group. Scale bars represent 10 μ m (A and B), 5 μ m (C–E), 1 μ m (H, bottom row), 500 nm (H, top row), and 20 μ m (J). AU, arbitrary units. *, $P < 0.05$.

of adult mice, we assessed laminin localization in inner medullary CDs of control and $Hoxb7:Rac1^{f/f}$ mice. There were no obvious differences in basal laminin ($\alpha 1$ subunit) localization between controls and mutants (Fig. 3 J), indicating that in CDs $Rac1$ -dependent epithelial polarity is likely not controlled by autocrine basal laminin assembly.

Rac1 is required for CD cell tubulogenesis

Our in vivo findings suggest that deleting $Rac1$ in the CD results in a mild branching morphogenesis defect, abnormal CD development, and marked epithelial structural and physiological defects in adult mice. To determine the mechanism of these defects, we isolated CD cells from 8-wk-old $Rac1^{f/f}$ mice and deleted $Rac1$ in vitro using adenoviral-mediated delivery of a plasmid encoding Cre recombinase. We generated cells that did not express $Rac1$ ($Rac1^{-/-}$), and deletion was verified by immunoblotting (Fig. 4 A). Based on the in vivo epithelial morphogenesis defects in the kidney, we initially defined the role of $Rac1$ in an in vitro three-dimensional CD tubulogenesis assay. Unlike $Rac1^{f/f}$ CD cells which form branched tubules, $Rac1^{-/-}$ CD cells formed multicellular cysts (Fig. 4 B). We next defined which crucial cell functions required for tubulogenesis, such as cell adhesion, migration, and spreading, were affected by $Rac1$ deficiency. $Rac1^{-/-}$ CDs had severe adhesion, spreading and migration defects when placed on Matrigel (MG; Fig. 4, C–F), suggesting these cells were unable to form focal adhesions. This was confirmed by performing immunofluorescence studies for phospho-paxillin on cells spread on MG (Fig. 4, G and H). Since integrins are required for cell adhesion and they regulate adhesion-dependent signaling pathways we performed in vitro replating assays to assess the ability of $Rac1^{-/-}$ cells to activate focal adhesion kinase (Fak), Akt, Erk, and p38-MAPK (Yazlovitskaya et al., 2015). No differences were noted between control and $Rac1^{-/-}$ CDs (Fig. 4, I and J). We also verified that the adhesion defects were not due to differences in surface expression of integrins by performing flow cytometry for the major integrin subunits ($\beta 1$, $\alpha 1$, $\alpha 2$, $\alpha 3$, and $\alpha 6$). In fact, the only difference between $Rac1^{f/f}$ and $Rac1^{-/-}$ CD cells was increased expression of the $\alpha 2$ subunit in the mutant $Rac1^{-/-}$ cells (Fig. 4 K). Finally, we defined whether the $\beta 1$ integrin in the $Rac1^{-/-}$ cells was active by determining the binding of antibody 9EG7 (which binds to the active form) relative to the total number of $\beta 1$ integrins as defined by binding to a non-conformational antibody (Ha2/5). There was no difference in the integrin activation status (9EG7 to Ha2/5 ratio) between

$Rac1^{-/-}$ and $Rac1^{f/f}$ CD cells (Figs. 4 K and S2 A). Thus, $Rac1$ deletion in CD cells leads to significant epithelial tubulogenesis, adhesion, spreading, and migration defects that are not due to integrin activation or integrin-dependent signaling abnormalities. This suggests that the phenotype was due to abnormalities within the actin cytoskeleton.

Rac1 is required for CD cell polarity and cytoskeletal organization

We used the $Rac1^{-/-}$ CD cells to understand the mechanism underlying the in vivo polarity defect in $Hoxb7:Rac1^{f/f}$ mice. Like the mice, there was a marked decrease of total and membrane levels of E-cadherin, ZO-1, and AQP2 in $Rac1^{-/-}$ CD cells (Fig. 5, A and B). This was verified by confocal microscopy in polarized $Rac1^{-/-}$ CD cells grown to confluence on transwell inserts. The amount of apical ZO-1 was markedly reduced, resulting in a significantly reduced polarization index (Fig. 5, C and D). There was a complete loss of the junctional E-cadherin pattern in $Rac1^{-/-}$ CD cells in z-stacks and apical cross sections (Fig. 5 C). $Rac1^{-/-}$ CD cells were also unable to normally localize AQP2 to the apical membrane (Fig. 5, E and F). Like the in vivo phenotype, $Rac1^{-/-}$ CD cells also showed a defect in polarized actin cytoskeletal organization, as they were unable to concentrate Ezrin in the apical domain (Fig. 5, G and H), indicating polarized cytoskeletal disruption. Indeed, phalloidin-rhodamine-labeled monolayers of $Rac1^{-/-}$ CD cells show a near-complete loss of the dense apical F-actin network (Fig. 5, I and J). These data indicate that $Rac1^{-/-}$ cells had a major polarity defect due to alterations in the actin cytoskeleton.

Rac1 controls CD epithelial functions independent of its major downstream effector Pak1

To define how $Rac1$ mechanistically controls CD cytoskeletal organization, which is required for epithelial cell polarization and function, we initially investigated signaling via its major cytoskeletal effector Pak1. The ability of $Rac1$ to activate its effectors requires membrane binding sites that are components of cholesterol-rich membrane domains (del Pozo et al., 2004; Symons, 2011). We therefore determined the surface expression of the lipid raft marker ganglioside GM1 by flow cytometry and showed that it was significantly reduced in $Rac1^{-/-}$ CDs, suggesting defective $Rac1$ -Pak1 signaling (Fig. 6 A). Integrin-mediated $Rac1$ activation leads to Pak1 autophosphorylation, so we performed a cell replating assay to assess Pak1 activation in $Rac1^{-/-}$ CD cells, and we assessed Pak1 activation in vivo in

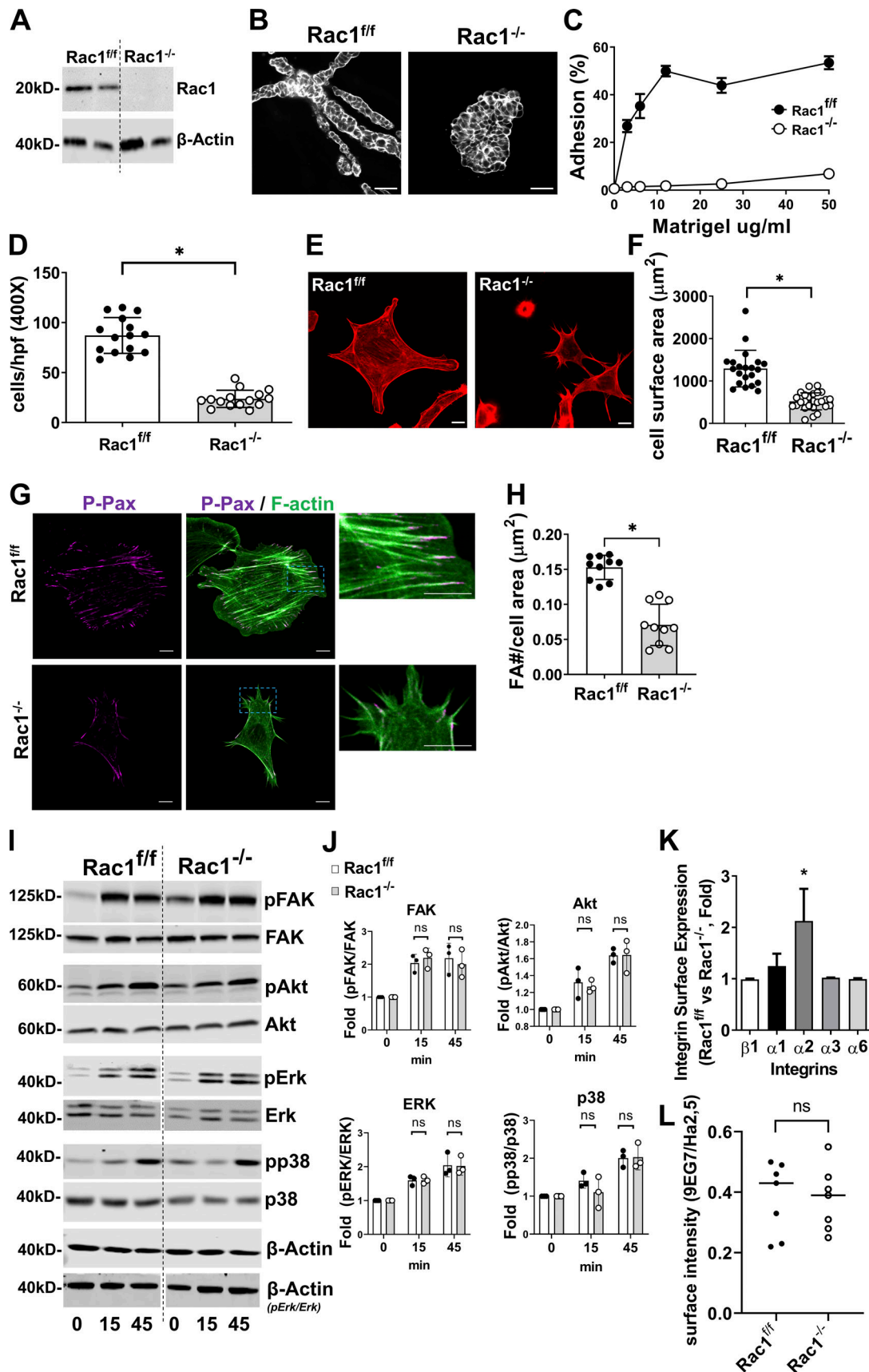


Figure 4. **Rac1^{-/-} CD cells have tubulogenesis, adhesion, migration, and spreading defects despite normal integrin function.** (A) Rac1 expression in adenoCre-treated Rac1^{ff/ff} CD cells (Rac1^{-/-}) was analyzed by immunoblotting. (B) Confocal image of tubule formation in a 3D MG gel of CD cells stained with

rhodamine-phalloidin. **(C)** CD cell adhesion to different concentrations of MG at 1 h after plating was measured. Shown are means \pm SEM. **(D)** CD cell transmigration across transwells coated with MG (20 $\mu\text{g}/\text{ml}$) was evaluated after 4 h from plating. Shown are individual values and means \pm SD of 15 high-power fields per group. hpf, high-power field. **(E and F)** $\text{Rac1}^{\text{fl/fl}}$ and $\text{Rac1}^{-/-}$ CD cells were plated on MG and allowed to spread for 1 h, after which they were stained with rhodamine-phalloidin (E) and the spreading area was quantified using ImageJ. Mean \pm SD and individual values of at least 20 cells are shown. **(G and H)** CD cells plated on MG for 1 h were immunostained with phospho-paxillin (P-Pax; magenta) and costained with rhodamine-phalloidin (green; G) and the focal adhesion number was counted using ImageJ and normalized to the cell area with values shown in mean \pm SD of 10 individual cells (H). **(I and J)** $\text{Rac1}^{\text{fl/fl}}$ and $\text{Rac1}^{-/-}$ CD cells were either left in suspension or plated onto MG for 15 and 45 min and then immunoblotted for phosphorylated (p) and total FAK, Akt, Erk, and p38-MAPK or β -actin to verify equal protein loading (I). Three repeat experiments were quantified using densitometry (J) and shown as individual values and mean \pm SD. The vertical white line for Erk/pErk separates samples that were rearranged from the same blot with a separate loading control as indicated. **(K and L)** Surface expression of integrin β 1, α 1, α 2, α 3, and α 6 subunits was analyzed by FACS in $\text{Rac1}^{\text{fl/fl}}$ and $\text{Rac1}^{-/-}$ CD cells by using R-phycoerythrin conjugated secondary antibodies and shown as between-group fold change for each subunit as mean \pm SD (K). Integrin activation was quantified by immunofluorescence staining for activated (9EG7) and total (Ha2/5) β 1 integrins and calculating the surface ratio using ImageJ (L), and values represent mean \pm SEM. A minimum of three experiments were performed throughout. Scale bars represent 50 μm (B) and 5 μm (E and G). *, $P < 0.05$.

isolated renal papilla of $\text{Rac1}^{\text{fl/fl}}$ and $\text{Hoxb7}:\text{Rac1}^{\text{fl/fl}}$ mice. As expected, $\text{Rac1}^{\text{fl/fl}}$ cells showed strong autophosphorylation of Pak1 after adhering to MG, but this was undetectable in the $\text{Rac1}^{-/-}$ CD cells (Fig. 6, B and C). Similarly, Pak1 activation was decreased in vivo in $\text{Hoxb7}:\text{Rac1}^{\text{fl/fl}}$ mutant papilla (Fig. 6, D and E). To define whether the abnormal phenotypes in the $\text{Rac1}^{-/-}$ CD cells were due to the inability to activate Pak1, we treated them with FTY720, a synthetic sphingosine-like analogue with the ability to, among other things, directly activate Pak1 via a Rho GTPase-independent mechanism (Bokoch et al., 1998; Ke et al., 2013; Liu et al., 2011). FTY720 restored Pak1 phosphorylation in the replating assay to a level that was comparable to $\text{Rac1}^{\text{fl/fl}}$ cells (Fig. 6, F and G); however, it failed to rescue the $\text{Rac1}^{-/-}$ CD cell spreading, migration, adhesion, and polarity defects (Fig. 6, H–L). Additionally, FTY720 was unable to restore apical actin cytoskeletal organization in polarized $\text{Rac1}^{-/-}$ CD cells (Fig. 6, M and N). These results show that global stimulation of Pak1 is unable to rescue the epithelial integrity defects of $\text{Rac1}^{-/-}$ CD epithelial cells. Thus, although Rac1 activates Pak1 in CD cells, it is unlikely to be the key Rac1-dependent regulator of CD cell integrity.

The WAVE2–Arp2/3 actin nucleation apparatus is defective in Rac1 -null CDs

We next defined whether the $\text{Rac1}^{-/-}$ cells altered RhoA and Cdc42 signaling, as these two small GTPases are also major mediators of actin cytoskeleton dynamics. Surprisingly, they were not differentially activated, as defined by the cdc42-GTP and RhoA-GTP pull-down assays performed on $\text{Rac1}^{\text{fl/fl}}$ and $\text{Rac1}^{-/-}$ CD cells plated on MG (Fig. S2, B and C). Another mechanism whereby signaling downstream of Rac1 can alter the actin cytoskeleton is by its direct ability to stimulate the WAVE2–Arp2/3 signaling axis (Chen et al., 2017). To become active, WAVE2 is phosphorylated at tyrosine 150 within the WAVE regulatory complex, which leads to release of its VCA domain, which in turn binds to and activates the Arp2/3 complex that nucleates and polymerizes actin at branching points (Leng et al., 2005; Mendoza, 2013). To assess whether alterations in actin dynamics caused the functional impairment of the $\text{Rac1}^{-/-}$ CD cells, we treated them with the synthetic polyamine C8N6-BPA, which reduces the turnover of actin and enhances nucleation of actin at the cell edge to generate lamellipodia (Nedeva et al., 2013; Riveline et al., 2014). C8N6-BPA increased the number of cells with lamellipodia and spreading area in

$\text{Rac1}^{\text{fl/fl}}$, but not $\text{Rac1}^{-/-}$, CD cells, indicating a defect of actin nucleation and branching (Fig. 7, A–C). We therefore assessed whether this was caused by a defect in the WAVE2–Arp2/3 complex by determining the level of phosphorylated and total WAVE2 and total Arp2/3 levels in replated CD cells. The total amount of WAVE2 and its phosphorylation level were significantly decreased, as were the total amounts of Arp2 and Arp3 in $\text{Rac1}^{\text{fl/fl}}$ relative to $\text{Rac1}^{-/-}$ CD cells (Fig. 7, D and E). Consistent with the in vitro data, we also observed decreased WAVE2 and total Arp2 in the $\text{Hoxb7}:\text{Rac1}^{\text{fl/fl}}$ papilla in vivo (Fig. S2, D and E). In epithelial monolayers, Arp2/3 localizes to cell–cell junctions to provide stability by creating a branched actin network (Efimova and Svitkina, 2018; Lee et al., 2016; Verma et al., 2012). We stained CD monolayers in vitro for Arp2 and performed line scans to assess its junctional localization. Apical cross sections of $\text{Rac1}^{-/-}$ CD epithelial layers demonstrated that Arp2 was less tightly associated with junctional F-actin, and the junctional peak in the line-scan analysis was abolished in addition to an overall decrease of junctional Arp2 (Fig. 7, F–H). To test whether the Arp2/3 deficiency caused the actin cytoskeletal defects, we performed pyrene-actin polymerization assays on cellular extracts of $\text{Rac1}^{\text{fl/fl}}$ and $\text{Rac1}^{-/-}$ CD cells. $\text{Rac1}^{-/-}$ cellular extracts are unable to appreciably induce actin polymerization (Fig. 7, I and J). The purified VCA domain (of Wiskott–Aldrich syndrome proteins such as WAVE2), which is known to stimulate actin polymerization in an Arp2/3-dependent manner, had no effect on $\text{Rac1}^{-/-}$ cellular extracts, whereas polymerization in $\text{Rac1}^{\text{fl/fl}}$ extracts was markedly increased (Fig. 7, I and J). Reconstitution by adding purified Arp2/3 complex in addition to VCA to $\text{Rac1}^{-/-}$ extracts did, however, restore polymerization to VCA-stimulated levels of $\text{Rac1}^{\text{fl/fl}}$ cells (Fig. 7, I and J). These data indicate that Rac1 is required for stabilization and functional activity of the WAVE2–Arp2/3 actin nucleation apparatus in CD cells.

Actomyosin is dysregulated in $\text{Rac1}^{-/-}$ CD cells

Arp2/3-dependent actin cytoskeletal networks are required for normal myosin II activity (Schell et al., 2018; Yang et al., 2012). We therefore investigated the actomyosin activation status in CD cells and the CD. We initially immunoblotted for phosphorylated myosin light chain (p-MLC) in CD cells in vitro and papillary extracts from 4-mo-old mice in vivo. $\text{Rac1}^{-/-}$ CD cells and $\text{Hoxb7}:\text{Rac1}^{\text{fl/fl}}$ papilla had significantly increased p-MLC levels compared with controls, indicating increased actomyosin activity (Fig. 8, A

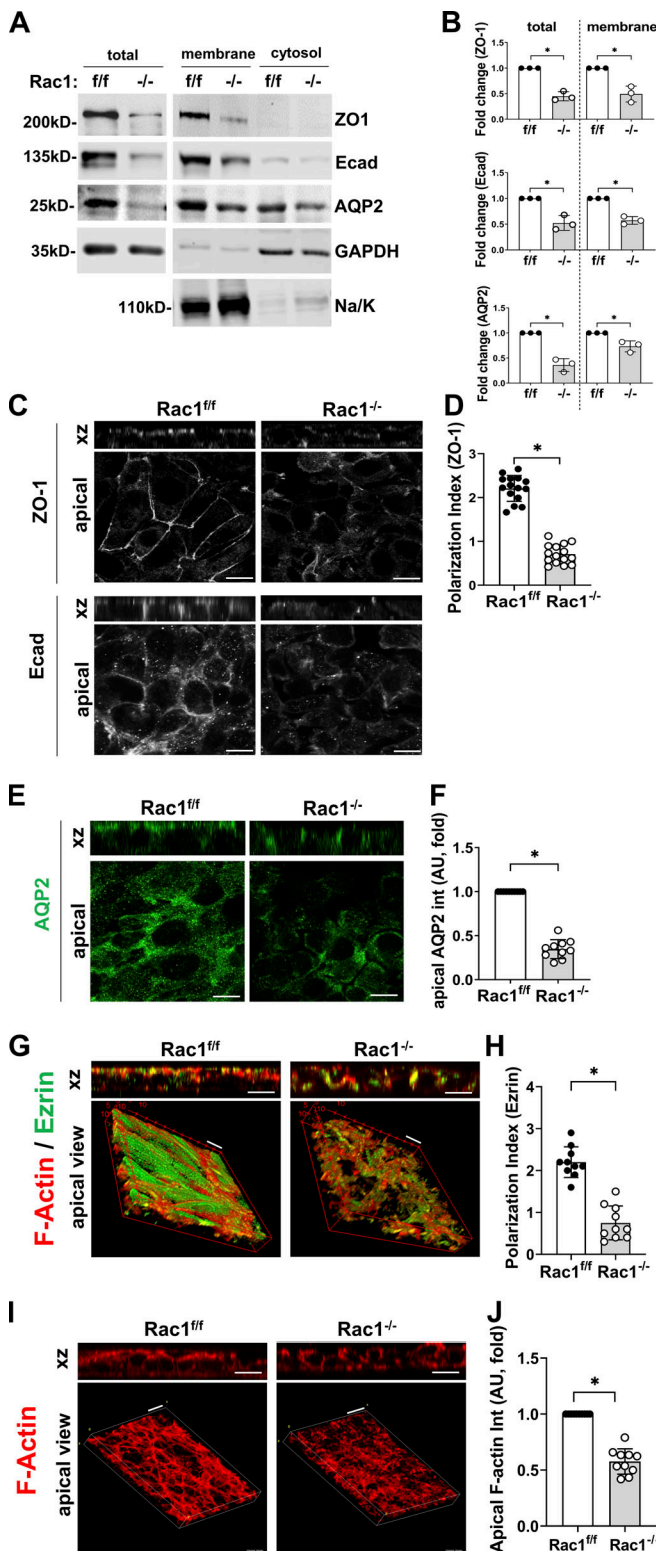


Figure 5. *Rac1*^{-/-} CD monolayers have a defect in polarity and cytoskeletal organization. (A and B) Equal amounts of whole-cell lysates as well as membrane and cytosol fractions from *Rac1*^{ff} and *Rac1*^{-/-} CD cells were immunoblotted for ZO-1, E-cadherin (Ecad), and AQP2. Na/K-ATPase and GAPDH were used to verify fraction purity. A representative immunoblot is shown (A), and experiments were quantified using densitometry (B) and shown as individual values and mean ± SD. (C–F) *Rac1*^{ff} and *Rac1*^{-/-} CD cells were grown to confluent monolayers in transwells; immunostained for ZO-1,

and B). We next measured the myosin content in the actin cytoskeletal fraction of CD cells using a modified triton solubility assay (Sato et al., 2017). Indeed, myosin light chain (MLC) was enriched in the cytoskeletal and depleted in the cytosolic fractions of *Rac1*^{-/-} CD cells compared with controls, confirming increased actin-myosin binding (Fig. 8, C and D).

When we assessed the distribution of increased contractility (p-MLC) in F-actin-labeled single CD cells by immunofluorescence, it was strikingly increased at the edge of *Rac1*^{-/-} CD cells. This was confirmed by line-scan profiling, and it indicates increased peripheral contractility (Fig. 8, E and F; Schell et al., 2018). In epithelial cells, actomyosin is enriched at apical cell-cell junctions, and it is critical for apicobasal polarization (Ivanov et al., 2010; Quiros and Nusrat, 2014; Salomon et al., 2017). There was a decrease in apical and an increase in basal p-MLC in *Rac1*^{-/-} cells (Fig. 8 G), which was quantified using mean intensities of monolayers sectioned through the z axis (Fig. 8 H). To functionally assign a role for Arp2/3 in the *Rac1*-dependent actomyosin dysregulation, we treated WT CD cells with the Arp2/3-specific inhibitor CK666. This inhibitor mimicked *Rac1* deficiency by causing spreading, focal adhesion, polarization, and actin cytoskeletal defects that are paralleled by increased MLC phosphorylation and p-MLC redistribution to the cell edge (Fig. S3). Together, these results show that *Rac1* is required to restrict actomyosin activity in polarized CD epithelial cells, presumably by stabilizing Arp2/3-dependent branched actin networks.

Direct myosin II inhibition rescues the epithelial defects of *Rac1*^{-/-} CD cells

We next defined whether *Rac1*-dependent Arp2/3-controlled actin cytoskeletal stability restricts myosin-mediated cellular contractility. Myosin motor activity is modulated by MLC phosphorylation, which is in turn regulated by MLC kinase (MLCK) or Rho kinase. Since RhoA was not up-regulated in *Rac1*^{-/-} CD cells (Fig. S2, B and C), we focused on inhibiting MLCK using a potent selective inhibitor, ML-7 (Xiong et al., 2017). ML-7 moderately but significantly reduced spreading, migration, and polarization in *Rac1*^{ff} CD cells, likely indicating either well-known off-target effects of MLCK inhibition or that some myosin phosphorylation is required for basic epithelial function (Fig. S4; Connell and Helfman, 2006). However, ML-7 had no effect on the phenotype of *Rac1*^{-/-} CD cells, suggesting that MLCK-dependent myosin phosphorylation is unlikely to be the key mechanism downstream of *Rac1* (Fig. S4) and that it is

E-cadherin, and AQP2; and analyzed by confocal laser scanning microscopy with z-stacking. Shown are representative z-stacks in xz dimension (top panels) and apical cross sections (bottom panels). The polarization index (D) was quantified as described in Materials and methods, and apical AQP2 intensity (F) was quantified using ImageJ. (G–J) *Rac1*^{ff} and *Rac1*^{-/-} CD monolayers were immunostained for Ezrin (green), and F-actin was labeled with rhodamine-phalloidin (red). Shown are confocal z-stacks in xz dimension (top panels) and 3D reconstructions (bottom panels). 3D reconstructions and quantifications of apical staining intensities (H and J) were done with ImageJ/Fiji with either the 3D or volume viewer plugin. Shown are representative images, and quantifications (D, F, H, and J) are in mean ± SD of at least 10 individual fields. A minimum of three experiments were performed throughout. Scale bars represent 10 μm (C, E, and G) and 15 μm (I). *, P < 0.05.

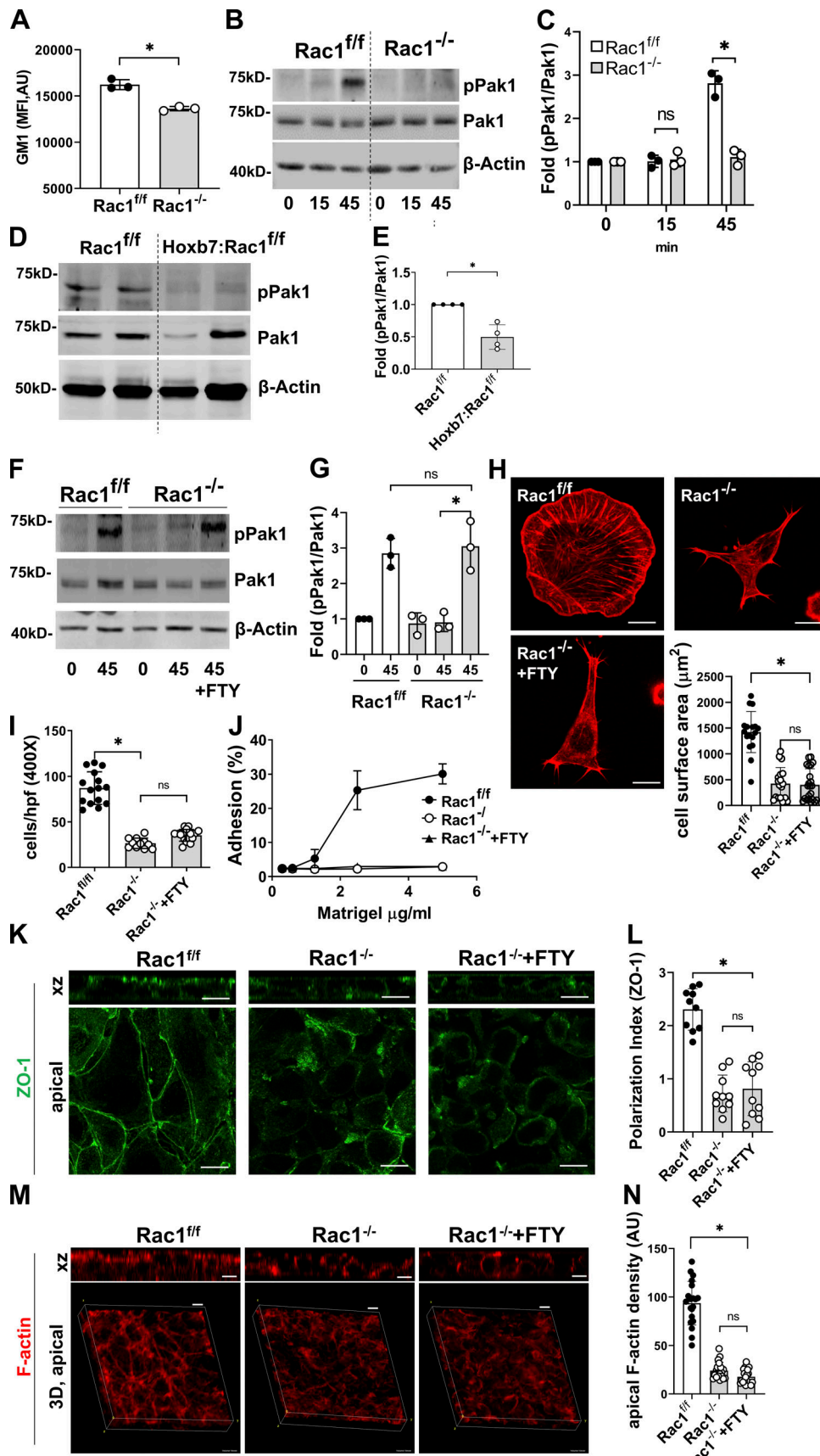


Figure 6. Morphological defects of *Rac1*^{-/-} CD cells are not mediated by Pak1. (A) Surface expression of the lipid raft marker ganglioside GM1 was analyzed in *Rac1*^{ff/ff} and *Rac1*^{-/-} CD cells by flow cytometry using FITC-conjugated cholera toxin B subunit. Shown is the mean fluorescence intensity (MFI); mean

± SEM). **(B–E)** CD cells were either left in suspension or plated onto MG for the times indicated (min) and cell lysates were analyzed for levels of phosphorylated and total Pak1 (B). Renal papilla of adult (6 mo) *Rac1^{fl/fl}* and *Hoxb7:Rac1^{fl/fl}* mice were immunoblotted for phosphorylated and total Pak1 (D). Experiments or individual mice were quantified using densitometry and shown as individual values and mean ± SD in (C and E). **(F and G)** CD cells were treated with the Pak1 inducer FTY720 (1 μM) during replating on MG. Cells were harvested after 45 min, and levels of phosphorylated and total Pak1 were analyzed by immunoblotting (D). Experiments were quantified using densitometry and shown as individual values and mean ± SD (E). **(H–J)** *Rac1^{fl/fl}*, *Rac1^{-/-}*, and FTY720-treated *Rac1^{-/-}* CD cells were plated on MG for 1 h and then stained with rhodamine-phalloidin to assess spreading (H), which was quantified in using ImageJ and shown as mean ± SD of at least 10 cells individual cells. Migration (4-h transwell assay toward MG) was analyzed and shown as mean ± SD of at least 10 fields (I), and adhesion on different concentrations of MG is shown as mean ± SEM of three experiments (J). **(K–N)** *Rac1^{fl/fl}*, *Rac1^{-/-}*, and FTY720-treated *Rac1^{-/-}* CD cells grown to confluent monolayers in transwells were immunostained for ZO-1 (K, green) or labeled with rhodamine-phalloidin (M, red) and analyzed with confocal laser scanning microscopy. The polarization index was calculated using ImageJ as indicated in Materials and methods (mean ± SD; L). Shown are z-stacks in xz dimension (top panels, K and M) and apical cross sections (bottom panels, K) or 3D reconstructions of F-actin (bottom panels, M; ImageJ/Fiji volume viewer) with apical F-actin quantified in N (a minimum of 20 measurements shown; mean ± SD). A minimum of three experiments were performed throughout. Scale bars represent 10 μm (H, K, and M). *, *P* < 0.05.

insufficient to reduce *Rac1*-dependent hypercontractility. We therefore directly inhibited myosin II using low-dose blebbistatin (5 μM, which inhibits ~50% of cellular contractility), which blocks myosin and keeps myosin heads in a low actin-affinity state (Doyle et al., 2015; Rauscher et al., 2018). Low-dose blebbistatin fully restored spreading, partially restored migration, and fully restored adhesion and focal adhesion formation in *Rac1^{-/-}* CD cells (Fig. 8, I–K; and Fig. S5, A–C). Similarly, polarization, as indicated by the tight junction marker ZO1, apical Ezrin and apical AQP2 localization were restored in blebbistatin treated *Rac1^{-/-}* CD cells (Fig. 8, L and M). Thus, *Rac1* dependent stabilization of Arp2/3-branched actin networks directly control actomyosin contraction, which regulates CD epithelial integrity.

Rac1 controls epithelial morphology by maintaining lateral F-actin height and lateral membrane stability

Branched Arp2/3-dependent actin networks at lateral cell–cell borders are critical for normal actomyosin activity, lateral cell–cell junction stability, and normal epithelial morphology (Efimova and Svitkina, 2018; Li et al., 2020). Given that *Rac1* in CD cells promotes Arp2/3 branched actin networks and restricts actomyosin, we examined whether *Rac1* is required for normal epithelial morphology and lateral membrane integrity. To characterize epithelial morphology *in vivo* in greater detail, we isolated fresh-frozen papilla, which contains inner medullary CDs of columnar to cuboidal morphology (Qiao et al., 1999). We performed thick cryo-sectioning combined with optical clearing for full confocal 3D visualization of phalloidin-labeled collecting ducts. Longitudinal as well as transverse cross sections revealed that mutant (*Hoxb7:Rac1^{fl/fl}*) epithelial cells have decreased apical F-actin density and decreased lateral F-actin height (Fig. 9, A–C), causing the epithelial cells to be shorter and more rounded and have apical invaginations at cell–cell junctions, which was confirmed with TEM (Fig. 9, D and E). Furthermore, TEM of papillary *Hoxb7:Rac1^{fl/fl}* epithelium revealed detaching lateral cell–cell contacts in *Hoxb7:Rac1^{fl/fl}* CDs, indicating compromised lateral membrane integrity (Fig. 9 F). This correlated with increased actomyosin activity (p-MLC) along the apicobasal axis, with more activated myosin II basolaterally in mutant *Rac1*-deficient epithelium compared with a more apical localization in controls (Fig. 9, G and H). These data suggest that *Rac1*-dependent restriction of actomyosin along lateral membranes is required to maintain normal epithelial cell height, lateral membrane integrity, and overall morphology *in vivo*.

Rac1 promotes lateral actin dynamics and restores lateral F-actin and normal morphology

Since *Rac1* is critical to maintain normal lateral F-actin and CD epithelial morphology, we next asked whether *Rac1* also actively promotes lateral actin dynamics and restoration of epithelial morphology. To assess whether *Rac1* controls lateral actin dynamics at cell–cell contacts in live CD cells, we performed FRAP of live SiR-actin-labeled *Rac1^{fl/fl}* and *Rac1^{-/-}* cells. We bleached F-actin at lateral sites of initial cell–cell contact formation in newly forming monolayers (Fig. 9 I). Lateral F-actin of *Rac1^{-/-}* CD cell layers recovers significantly slower than controls, indicating impaired actin dynamics at lateral membranes (Fig. 9, I and J). Next, to test whether the lateral F-actin defects are functionally relevant for morphological restoration, we assessed lateral F-actin height in regenerating CD cell layers *in vitro*. For this, we performed a scratch assay of confluent CD cells and imaged areas adjacent to the scratch as soon as they were covered with cells of comparable density (Fig. S5, D and E). This took significantly longer for mutant cells given the known migration defect (Fig. S5, D and E). F-actin of regenerating control CD layers was restored to a tight network across cell–cell junctions (apical cross sections), and lateral F-actin reached full epithelial cell height, leaving no apical invaginations (in xz dimension; Fig. 9 K). *Rac1^{-/-}* CD epithelial cell layers, however, demonstrated incomplete regeneration, with defective F-actin at cell–cell junctions and shorter lateral F-actin with apical invaginations at cell–cell junctions (Fig. 9, K and L). This was inducible in control cells with Arp2/3 inhibition (CK666) and reversible in *Rac1^{-/-}* CD cells with actomyosin inhibition (blebbistatin), suggesting that Arp2/3 branched actin networks and restriction of actomyosin are likely causally involved in this *Rac1*-dependent restoration of lateral F-actin and epithelial morphology (Fig. 9, K and L). In summary, these data indicate that *Rac1*, by restricting actomyosin, not only maintains but also actively promotes lateral actin dynamics and restores epithelial morphology.

Discussion

Despite the overwhelming cell culture and organ explant evidence that *Rac1* plays a key role in epithelial tubulogenesis and branching of the lung and mammary gland (Danopoulos et al., 2016; Morrison et al., 2015; Tushir and D'Souza-Schorey, 2007; Zhu and Nelson, 2013), its role *in vivo* is unclear. Contrary to

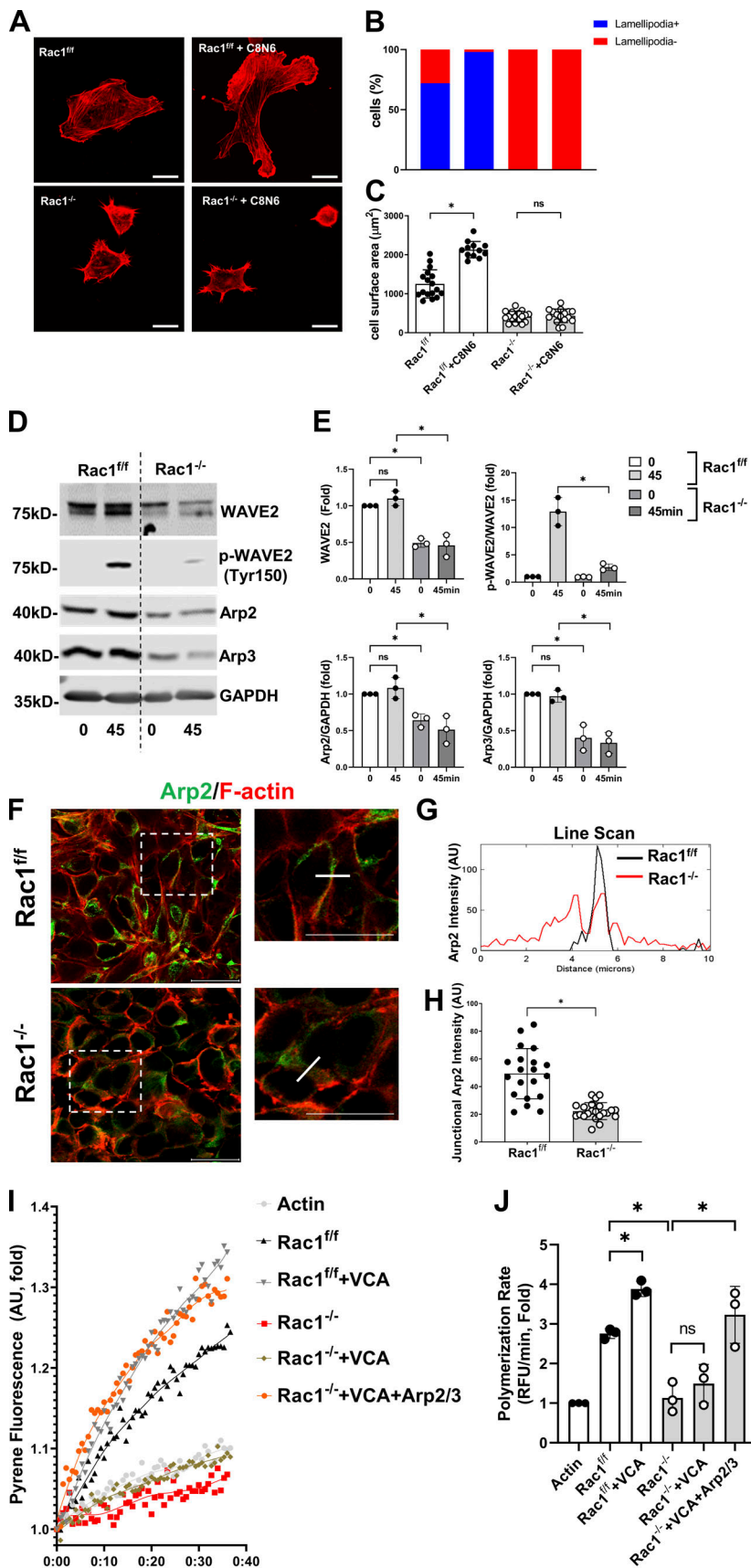


Figure 7. Rac1 deficiency causes a defect in the WAVE2-Arp2/3 actin nucleation apparatus. (A–C) Untreated or C8N6-BPA (C8N6, 100 nM)-treated CD cells were allowed to spread on MG for 1 h, labeled with rhodamine-phalloidin (red), and analyzed with confocal laser scanning microscopy (A). Lamellipodia, expressed as percentage of cells with lamellipodia (10 high-power fields were analyzed per experiment; B), and cell area (10 cells per experiment were analyzed, expressed as mean \pm SEM; C) were quantified using ImageJ/Fiji. **(D and E)** CD cells in suspension or replated on MG for 45 min were analyzed by immunoblotting for total and activated (pTyr150) WAVE2 and the actin nucleator complex subunits Arp2 and Arp3 (D). Quantification was done with densitometry using ImageJ (E; mean \pm SEM). **(F–H)** CD cell monolayers were immunostained for Arp2 (green), and F-actin was costained with rhodamine-phalloidin (red; F). Line-scan profiling was performed and indicated by the white dotted line in (F) and the plot profile function of ImageJ was used (G). Line-scan profiles are representative of three repeat experiments with 10 junctions analyzed per experiment. Junctional Arp2 intensity was quantified (H), with a minimum of 20 measurements shown (mean \pm SD). **(I and J)** CD cell lysate was added to the pyrene-actin polymerization assay together with purified Arp2/3 complex (10 nM) or VCA domain (400 nM). Kinetic pyrene fluorescence was recorded over the indicated time on a Spectramax iD3 plate reader. *Rac1^{-/-}* cell lysate is unable to induce actin polymerization but can be rescued by the addition of Arp2/3 complex and VCA domain. A representative plot is shown (I), and the actin polymerization rate was calculated as indicated in Materials and methods (J). A minimum of three experiments were performed throughout. Scale bars represent 10 μm (A) and 20 μm (F). *, $P < 0.05$.

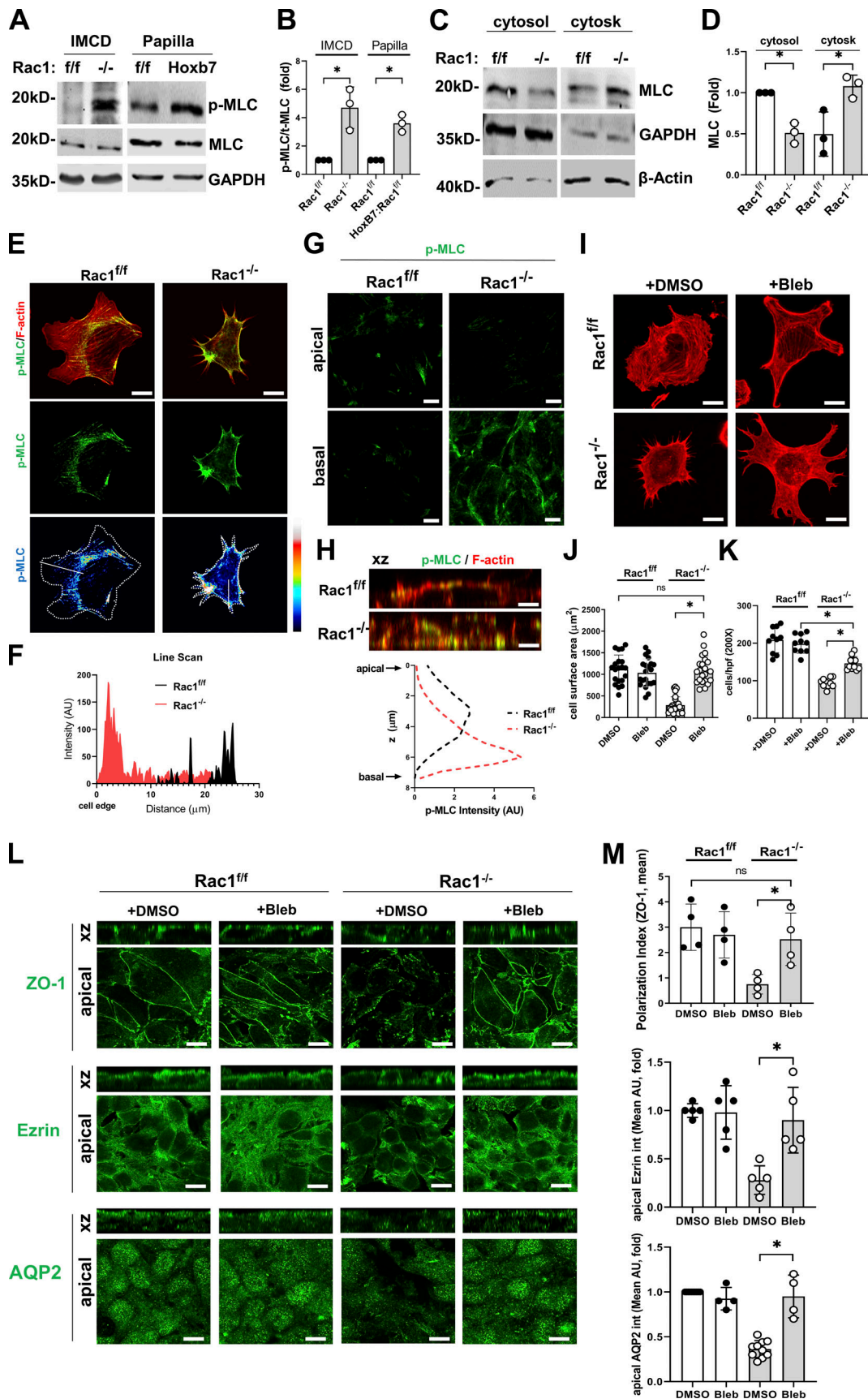


Figure 8. **Actomyosin is dysregulated in Rac1^{-/-} CD, and the epithelial defects are rescued by myosin II inhibition.** (A and B) Rac1^{f/f} and Rac1^{-/-} CD cellular lysates as well as Rac1^{f/f} (f/f) and Hoxb7:Rac1^{f/f} papillary lysates (Hoxb7) were immunoblotting for phosphorylated and total MLC. Quantification of

three samples per group is shown in B (mean \pm SD). IMCD, inner medullary collecting duct. **(C and D)** CD cell lysates were fractionated into the actin cytoskeletal and cytosolic fraction and subjected to immunoblotting for MLC. Quantification of repeat experiments (in mean \pm SD and as individual values) is shown in D. **(E and F)** CD cells were allowed to spread on MG for 1 h and immunostained for p-MLC (green) and costained with rhodamine-phalloidin (red; E). Line-scan analysis was performed as indicated by the white line in the bottom panels using the ImageJ/Fiji plot profile function, and a representative profile of repeats (10 cells/experiment) is shown in F. **(G and H)** CD confluent monolayers were immunostained for p-MLC (green) and costained with rhodamine-phalloidin (red) and analyzed with confocal laser scanning microscopy with z-stacking. Representative apical and basal cross sections are shown in G, and representative z-stacks in xz dimension are shown in H. A representative apicobasal Z-profile generated with ImageJ's Z-profile function is shown in H. **(I–K)** CD cells were treated with low-dose blebbistatin (5 μ M) and allowed to spread on MG for 1 h (I and J) or subjected to a 4-h transwell migration assay (K). Spreading area was measured and migrated cells were counted using ImageJ. Representative rhodamine-phalloidin-stained cells (I), and data (mean \pm SD) of repeat experiments are shown (J and K). Scatter plots indicate individual values of at least 20 cells (J) or 10 counted fields (K). **(L and M)** Blebbistatin (5 μ M)-treated CD confluent monolayers were immunostained for ZO-1, Ezrin, and AQP2 (all in green) and analyzed with confocal laser scanning microscopy with z-stacking (L). The polarization index and apical staining intensity were quantified using ImageJ. Values shown are mean \pm SD of repeat experiments (M). A minimum of three experiments were performed throughout. Scale bars represent 10 μ m (E, G–I, and L). *, $P < 0.05$.

expectations, we found that Rac1 did not play a major role in early branching morphogenesis of the renal collecting system, because it is only expressed once most branching is complete. We did, however, show that Rac1 is required to maintain epithelial integrity, polarity, morphology, and physiological function in adult kidneys. We further demonstrated that Rac1^{-/-} CD cells had severe adhesion and polarity defects, despite intact integrin function and signaling. These abnormalities were due to a major cytoskeletal defect, because Rac1 regulates WAVE2–Arp2/3–dependent actin cytoskeletal branching, which in turn controls actomyosin activity. Thereby Rac1 controls lateral F-actin height, lateral membrane integrity, and thus epithelial cell shape. We conclude that Rac1 maintains CD epithelial integrity and morphology by limiting cellular contractility via Arp2/3-dependent actin cytoskeletal branching (Fig. 10).

Rac1 is expressed late in CD development and its major role is to maintain adult epithelial polarity and function in the mature collecting system. This sharply contrasts with Cdc42, which is critical for UB branching morphogenesis, as demonstrated by the profound branching morphogenesis defect and early renal failure in Hoxb7:Cdc42^{-/-} mice (Elias et al., 2015). These incongruent results were unexpected, as Cdc42 and Rac1 regulate overlapping signaling pathways and cell functions, including epithelial polarity (Mack and Georgiou, 2014; Pichaud et al., 2019). While there is strong in vivo evidence that Cdc42 plays a critical role in branching morphogenesis in the kidney, lung, and mammary gland, very few studies have implicated Rac1 in epithelial cell branching morphogenesis (Bray et al., 2013; Elias et al., 2015; Wan et al., 2013). Rac1 was shown to be required for mammary branching morphogenesis in an ex vivo model by overexpressing constitutively active Rac1 and using a Rac1 inhibitor (Morrison et al., 2015). Similarly, Rac1 was shown to be required for lung branching morphogenesis using a Rac1 inhibitor ex vivo on lung explants in culture (Danopoulos et al., 2016). To the best of our knowledge, this is the first study examining the in vivo role of Rac1 in epithelial branching morphogenesis by its selective deletion in a developing mammalian organ. Nevertheless, the conflicting data from our study and those of others suggest that the role of Rac1 in branching morphogenesis is organ dependent. We can, however, conclude that Cdc42 plays a critical role in early branching morphogenesis of the kidney collecting system, while Rac1 predominantly plays a key role in CD maintenance in adulthood. This temporal differentiation of Rho GTPase requirements may be relevant in other organs.

We found that Rac1-deficient CD cells have defective adhesion, migration, and spreading despite normal integrin expression, activation, and signaling. These observations are like those found in mammary epithelial cells, where expression of dominant-negative Rac1 led to disorganized apical F-actin, disrupted E-cadherin, and decreased polarity but integrin localization remained undisturbed (Akhtar and Streuli, 2006). However, our results showing intact integrin signaling and activation in the context of Rac1 deficiency contrast with a study showing loss of integrin α 6 expression in hair follicles upon selective deletion of Rac1 in keratinocytes (Chrostek et al., 2006). Furthermore, platelet-specific Rac1 deletion causes defective glycoprotein Ib-IX (GPIb-IX) complex induced surface integrin α Ib β 3 activation (Delaney et al., 2012). Finally, in contrast to our data, the integrin–Rac1 signaling axis regulates canonical MAPK, p38, and Akt signaling that is important for transformation and invasiveness in various cancer epithelial cells (Kim et al., 2008; Wang et al., 2010). Hence, the effects of Rac1 on integrin expression and signaling appear to be cell-type specific and may differ between normal and transformed epithelial cells.

When we investigated the mechanisms underpinning the severe adhesion and polarity defects in Rac1^{-/-} CD cells, we found they were not mediated by abnormal signaling of the major Rac1 effector Pak 1. This result contrasts with other studies in both mesenchymal and epithelial cells where Pak1 controls various downstream cellular processes, including actin cytoskeletal turnover, adhesion, migration, and apicobasal polarization (deLeon et al., 2012; Tu et al., 2016). To this end, Pak1 and α PKC constitute a key dual-kinase mechanism that controls epithelial cell polarization when activated by Cdc42 (Aguilar-Aragon et al., 2018). These discrepant data imply that the downstream effects of Pak1 are highly dependent on the context, cell type, and activating upstream Rho GTPase.

We found that Rac1 deficiency induced a quantitative and functional deficiency of the WAVE2–Arp2/3 actin nucleation apparatus and that Arp2/3 inhibition impaired adhesion, migration, spreading, and polarity, suggesting this was the mechanism whereby Rac1 deficiency induces these defects. Our findings extend previous data, where Arp2/3-dependent actin protrusions were shown to maintain cell–cell junctions in MDCK (Madin–Darby canine kidney) cell monolayers (Li et al., 2020). Arp2/3 was also shown to be required for tight junction formation in the skin, and Arp2/3-dependent branched actin

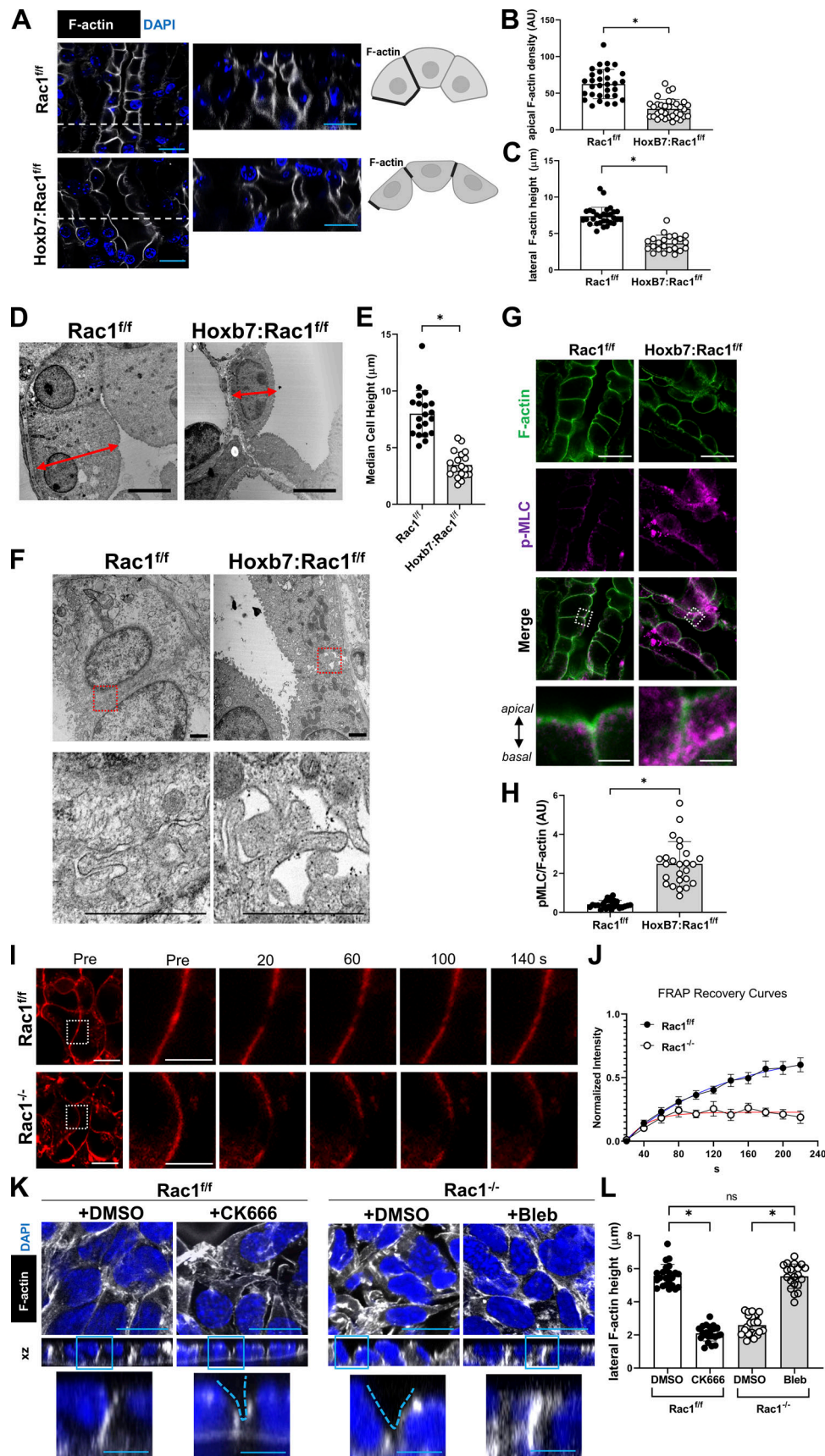


Figure 9. **Rac1 controls lateral F-actin, actin dynamics, and lateral membrane integrity, which is required for normal epithelial morphology.** (A–C) Thick frozen sections of renal papillae of *Rac1^{ff}* and *Hoxb7:Rac1^{ff}* mice were optically cleared and labeled with phalloidin (white) and DAPI (blue) and

analyzed with confocal microscopy (A). Z-stacks of a transverse (optical section shown as white dashed line) CD are shown on the right. (B and C) Apical F-actin and lateral F-actin height was quantified using ImageJ/Fiji. A minimum of 30 (B) or 20 (C) measurements is shown as scatter plot and mean \pm SD. (D and E) TEM of inner medullary CD epithelial cells in the papilla of *Rac1^{f/f}* and *Hoxb7:Rac1^{f/f}* mice showing cell height measurements (D), which was quantified and expressed as scatter plot (a minimum of 20 measurements shown) with mean \pm SD (E). *n* = 3 mice/group. (F) TEM of inner medullary collecting ducts in the papilla of *Rac1^{f/f}* and *Hoxb7:Rac1^{f/f}* mice showing regions of cell–cell contact (top panel) and a focused area highlighting the lateral cell membrane (bottom panel, red dashed box). (G and H) Frozen *Rac1^{f/f}* and *Hoxb7:Rac1^{f/f}* renal papillary sections were labeled with phalloidin-AF647 (green) and immunostained for p-MLC (magenta; G). Fluorescence intensity of p-MLC over phalloidin (F-actin) was quantified and expressed as scatter plot (a minimum of 25 measurements shown) with mean \pm SD (H). *n* = 3 mice/group. (I and J) FRAP of F-actin (SiR-actin, red) at lateral cell–cell contacts of *Rac1^{f/f}* and *Rac1^{-/-}* CD cells in vitro (I). Recovery after photobleaching was quantified and curve fitted (J), mean \pm SEM, *n* = 10. (K and L) Confluent *Rac1^{f/f}* and *Rac1^{-/-}* CD cells (treated with DMSO, CK666 100 μ M, or blebbistatin 5 μ M for 1 h before fixation) were wounded and allowed to migrate until cells had covered the highlighted scratch-adjacent areas as indicated in Fig. S5. Cells were then labeled with phalloidin-rhodamine (white) and (DAPI; K), and lateral F-actin height was quantified (L). *n* = 3 experiments and a minimum of 20 measurements (mean \pm SD) are shown in L. Scale bars represent 15 μ m (A and G), 3 μ m (G, inset), 4 μ m (D), 1 μ m (F), 10 μ m (I), 5 μ m (I, inset), 15 μ m (K), and 5 μ m (K, inset). *, *P* < 0.05.

networks maintain endothelial cell monolayer integrity (Efimova and Svitkina, 2018). In these studies, the upstream activator of the Arp2/3 complex was not defined. Although the Arp2/3 complex integrates multiple upstream signals depending on the environment and it is nonexclusive to Rac1 (Swaney and Li, 2016; Weaver et al., 2003), our studies do suggest that Rac1 may be a master regulator of Arp2/3-dependent functions in polarized epithelial cells. This appears to be epithelial cell specific, as Rac1-WAVE-Arp2/3 signaling was not required for fibroblast spreading or focal adhesion formation (Dimchev et al., 2021; Steffen et al., 2013). Interestingly, recent data recognize a cell type- and context-dependent subunit composition of the Arp2/3 complex that differentially regulates branched actin network characteristics (Abella et al., 2016; Pizarro-Cerdá et al.,

2017). Elucidating the cell type-dependent role of Rac1-Arp2/3-dependent actin cytoskeletal functions may improve our molecular understanding of disease processes caused by tissue-specific actin cytoskeletal disruption.

Our finding that Rac1-induced Arp2/3 branched actin networks constraining myosin II activity is a novel mechanism whereby epithelial cell polarity, morphology, and function are maintained. Since it would be technically challenging to reconstitute a branched actin network in the *Rac1^{-/-}* CDs, we cannot directly address the exact causal link. Using *Rac1^{-/-}* CD cells, we demonstrated excessive phosphorylation of MLC and binding of myosin to F-actin, which are key steps for actomyosin activation and surrogate endpoints for increased cellular contractility in nonmuscle cells (Zaidel-Bar et al., 2015). We found that direct inhibition of myosin II with blebbistatin reversed the epithelial defects, while modulation of MLC phosphorylation did not alter the phenotype. These data suggest that MLC phosphorylation is not the major mechanism whereby Rac1-Arp2/3 signaling regulates cellular contractility. Interestingly, others have demonstrated that Arp2/3-dependent actin networks can constrain myosin function independent of Rho kinase, a major kinase downstream of RhoA that modulates MLC phosphorylation (Yang et al., 2012). There is also evidence that an antiparallel actin filament arrangement can directly enhance myosin-dependent contractile activity and that Arp2/3 complex inhibition causes antiparallel actin fiber rearrangement, which directly triggers myosin incorporation into the actin network (Koestler et al., 2013; Reymann et al., 2012). Based on these data, we propose that in CD epithelial cells, Rac1 induces Arp2/3-dependent branched actin networks via WAVE2 that limit actin binding to myosin (Fig. 10). As the loss of Arp2/3-dependent branched actin networks has recently been associated with increased actomyosin activity, cellular hypercontractility, and disruption of cell junctions in podocytes, MDCK monolayers, and epidermal cells (Li et al., 2020; Schell et al., 2018; Zhou et al., 2013), we suggest this may be a generalized mechanism whereby Rac1 maintains epithelial cell integrity.

We demonstrate that Rac1 in mature epithelial cells in vivo controls lateral membrane F-actin and actomyosin activity, thereby maintaining lateral membrane integrity and overall epithelial morphology. This extends previous in vitro data showing that dynamic Arp2/3-dependent actin protrusions at lateral cell membranes are critical to prevent myosin-dependent contractility from constantly unzipping cell–cell adhesions

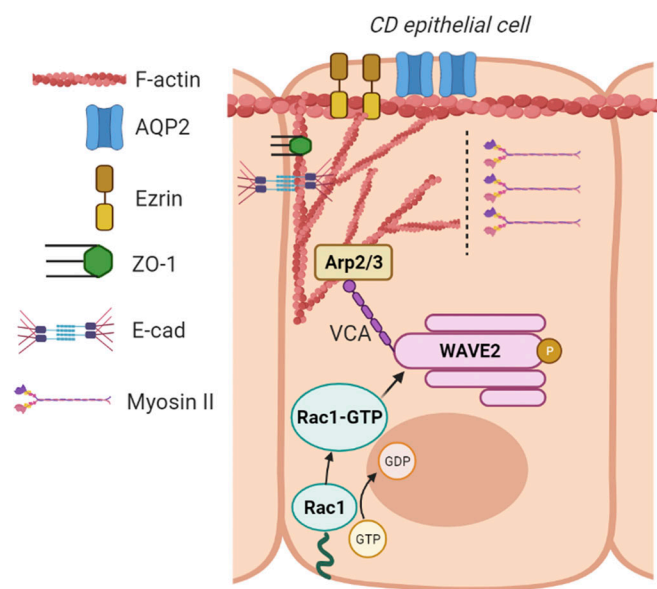


Figure 10. **Schematic representation of the role of Rac1 in CD epithelial cells.** Membrane-bound Rac1 is activated (Rac1-GTP) upon integrin binding to the ECM. Rac1-GTP directly binds to and activates the WAVE regulatory complex, leading to WAVE2 phosphorylation. This releases WAVE's VCA domain, which binds to the actin nucleation complex Arp2/3 to initiate actin polymerization at branching points. The Rac1-WAVE2-Arp2/3 axis generates a branched actin cytoskeleton, which restricts myosin II access to the cytoskeleton. This is required for apical cytoskeletal (Ezrin, and junction stability (ZO-1 and E-cadherin [E-cad]), which are critical for epithelial functions that require apicobasal polarization (water transport via AQP2) and to maintain epithelial morphology. Created with biorender.com.

(Li et al., 2020). Our data suggest that Rac1 is an upstream regulator of this critical process required to maintain tissue integrity. In the developing *Drosophila* pupal notum, it has long been established that Rac1 activity along an apicobasal gradient creates a polarized actin cytoskeleton and determines epithelial cell shape (Couto et al., 2017; Georgiou and Baum, 2010). Our data extend this function of Rac1 to a mature mammalian epithelial system in vivo and provide a mechanistic framework of how Rac1 maintains mature mammalian epithelial morphology.

Our data contrast studies that show Rac1-dependent epithelial morphology is largely determined by a Rac1-RhoA antagonism (Chauhan et al., 2011; Martin et al., 2016). These studies, however, used developmental systems of epithelial morphogenesis (e.g., the embryonic lens or *Caenorhabditis elegans* embryos), likely suggesting that Rac1-dependent mechanisms of maintaining mature mammalian epithelial cell shape differ. It is possible that epithelia at different ages use distinct molecular mechanisms to not only maintain but also restore morphology (e.g., after mechanical injury). In fact, in an in vitro injury model, we find that Rac1 promotes the restoration of lateral F-actin at cell-cell contacts to thereby promote the reestablishment of a normal morphology in a regenerating epithelial cell layer. Mechanical considerations of epithelial repair imply that the molecular mechanisms that shape the lateral membrane are likely fundamental in determining the regeneration of a differentiated epithelium (Tang, 2017). Future studies could elucidate whether Rac1 is a key player in modulating and restoring cell-cell interfaces during homeostasis or postinjury repair in other epithelial systems.

In conclusion, our study reveals a novel role for the canonical small Rho GTPase Rac1 in the kidney epithelium. Rac1 is not required for early CD epithelial development but instead maintains epithelial integrity and morphology in adults by maintaining epithelial cell polarity and function via Arp2/3-dependent branched actin networks, which restricts cellular contractility.

Materials and methods

Mice

All experiments were approved by the Vanderbilt University Institutional Animal Use and Care Committee and conducted in Association for Assessment and Accreditation of Laboratory Animal Care-accredited facilities. Rac1^{flox/flox} mice (Rac1^{f/f}), which were previously described (Chrostek et al., 2006), were crossed with Hoxb7Cre mice (gift of Andrew McMahon, Department of Stem Cell Biology and Regenerative Medicine, USC Keck School of Medicine, Los Angeles, CA; Yu et al., 2009). Mice were backcrossed onto the C57/B6 background (F7-10). Female and male mice were used in equal ratios, and aged-matched littermates (Rac1^{flox/flox}; Rac1^{f/f}) mice were used as controls.

Water deprivation

Mice undergoing metabolic studies were water deprived for 24 h. For acute water loading, mice were injected with 2 ml water intraperitoneally, followed by a second injection of 2 ml, 18 h after the first one. After the second injection, the mice were fluid restricted, and spot urine and body weight were collected at 2- to

6-h intervals. Urine osmolality was determined using freezing point depression as measured by an Advanced Instruments Osmometer, Model Osmol (Advanced Instruments). 3-h urine samples and volumes were obtained from mice with no access to water, while control 3-h urine was obtained from the same mice on a subsequent day with free access to water.

Generation of Rac1^{-/-} cells and culture

CD cells were isolated from Rac1^{f/f} mice following an established methodology (Husted et al., 1988). Intact kidneys from euthanized 6-8-wk-old mice were dissected and cut longitudinally and slightly off-center using a razor blade. Then, the whitish-colored T-shaped area (the medullary CD system) was lifted and removed. The tissue was minced and placed in sterile-filtered 1 mg/ml collagenase II (+5 mM CaCl₂) and dissolved in 1 ml 50 mM PBS, pH 7.4, in a 35-mm Petri dish. This was incubated for 1 h at 37°C, after which the cells were further suspended by vigorous pipetting. Then, complete medium (DMEM + 10% FBS + antibiotics) was added to the Petri dish, and the cells were washed, resuspended, and placed in a new 35-mm cell culture dish and kept in a 5% CO₂ incubator. Rac1 was deleted by infecting the cells with an adenoCre virus in vitro. Deletion of Rac1 was verified Western blot analysis. Clonal Rac1-null cell lines were generated, and similarity in their behavior was verified. Then, cells were transfected with pSV40 plasmid for immortalization. For cell treatments, all drugs were dissolved for stock solutions and used according to the manufacturer's recommendations. Solvents for stock solutions were used as negative control treatments in respective experiments.

Tubulogenesis assay

Tubulogenesis of CD cells was performed in 3D ECM gels composed of 0.1 mg/ml rat tail collagen I and MG in DMEM containing 20 mM Hepes (pH 7.2). For the MG/collagen gels, a 1:1 mixture of the collagen solution described above was mixed with growth factor-reduced MG, giving a final concentration of 0.5 mg/ml collagen and 0.5 mg/ml MG. CD cells (5 × 10³) were seeded into the gels, which were overlaid with 100 μl of 10% FCS full medium and allowed to grow for 5-7 d. The gels were stained with rhodamine-phalloidin, and the tubules were photographed using a Zeiss Axio 510 confocal microscope (400×).

Cell spreading and focal adhesion analysis

Slides coated with MG (20 μg/ml) were blocked with 2% heat-inactivated BSA for 1 h. Then, CD cells were plated in serum-free medium onto slides with the indicated treatments supplemented in the medium. After 1 h, cells were fixed with 4% paraformaldehyde and stained with rhodamine-labeled phalloidin. Images were collected with confocal microscopy (Leica TCS SPE or Zeiss LSM710, 780, or 880, objective 63×/1.4 NA Plan Apochromat oil), and the cell area was determined using ImageJ software. Focal adhesions were labeled by immunostaining for phospho-paxillin (Cell Signaling; #2541), and the number/cell area was quantified using ImageJ/Fiji.

Cell replating, adhesion, and migration assays

For replating, serum-starved CD cells were plated in serum-free medium on MG (20 μg/ml) for the indicated time points, after

which they were lysed and subjected to immunoblotting. For cell adhesions, 96-well plates were coated with different concentrations of MG and blocked with BSA. 10^5 cells in serum-free DMEM were placed in each well for 60 min; nonadherent cells were removed, and the remaining cells were fixed, stained with crystal violet, and solubilized. The optical density of the cell lysates was read at 540 nm. For migration, transwells with 8- μ m pores were coated with MG, and 10^5 cells were added to the upper well in serum-free medium. Treatments were supplied in serum-free medium throughout the assay. Cells that migrated through the filter after 4 h were stained with DAPI (Invitrogen; #P36935) and counted using ImageJ. Eight random fields were analyzed per each group or treatment using the following strategy. First, image background was subtracted and the threshold adjusted to only highlight nuclei. The image was then converted to a binary black/white image, and the particle analyzer function of ImageJ was used. Size or circularity were not restricted. For merged nuclei, a watershed function was applied. A minimum of three independent repeat experiments was performed.

Cell polarity and polarization index

Cells were grown on transwell inserts consisting of polyvinylpyrrolidone-free polycarbonate filters with 0.4- μ m pores (Corning; #3460). Confluent cells were fixed in 4% formaldehyde and incubated with antibodies directed against ZO-1, E-cadherin, Ezrin, or AQP2 followed by the appropriate FITC-conjugated secondary antibody, and rhodamine-phalloidin was supplemented in the antibody diluent for F-actin costaining. Chamber slides were mounted and viewed using a confocal microscope and analyzed using ImageJ or Leica LASX software. At least five regions of interest (ROIs) per group with a minimum size of 50 \times 50 μ m were defined. A minimum of 10 confocal z-stacks were acquired from each ROI during imaging. Apical immunofluorescence was quantified using ImageJ. The polarization index was quantified as previously described (Otani et al., 2019). Briefly, after background subtraction, an ROI was drawn around the apical plasma membrane, and the total intensity was measured. Then, the total intensity of the monolayer in its xz dimension was measured. The apical polarization index was determined by calculating the ratio of apical to total signal. Three independent repeat experiments were performed. For 3D reconstruction of immunostained or phalloidin-rhodamine-labeled CD monolayers, the volume viewer or 3D viewer plugin for ImageJ was used. For immunofluorescence profiling of proteins along the apicobasal axis, the Z-profile function of ImageJ/Fiji was used.

Western blotting and membrane fractionation

Cell lysates were prepared using M-PER reagent (Thermo Fisher; #78501). Lysates were centrifuged at 17,000 $\times g$ for 15 min at 4°C, and total protein concentration was determined using BCA reagent (Thermo Scientific). Lysates were resolved in 8%, 10%, or 12% SDS-PAGE depending on protein size and then transferred to nitrocellulose membranes. Membranes were incubated with the primary antibody listed below followed by IRDye fluorescent dyes secondary antibodies and a Li-Cor Biosciences Odyssey infrared imaging system. Immunoreactive

bands were quantified by densitometry analysis using ImageJ (National Institutes of Health) or Image Studio Lite. To quantify levels of protein phosphorylation, OD of bands for phosphoprotein was normalized to total protein or β -actin. For kidney tissue analysis, papilla were removed and mechanically lysed in T-PER reagent (Thermo Scientific) using a Polytron homogenizer, centrifuged, and then subjected to immunoblotting. The membrane and cytoplasmic fraction of CD cells was obtained by using the Cell Fractionation Kit (Cell Signaling; #9038) according to the manufacturer's protocol. Primary antibodies used are listed in Table S1. The secondary antibodies were IRDye 800CW Anti-Rabbit (#926-32213 and #926-32211), IRDye 800CW Anti-Mouse (#926-32212 and #926-32210), IRDye 680RD Anti-Rabbit (#926-68073 and #926-68071), and IRDye 680 Anti-Mouse (Li-Cor Biosciences; #926-68072 and #926-68070).

Integrin activation assay

Integrin activation was assessed on cells allowed to adhere to MG as described previously (Lu et al., 2016). The active conformation of integrin β 1 on adherent cells was determined using the 9EG7 antibody that specifically binds to the active conformation of integrin β 1. Total surface expression was determined using Ha2/5 antibody. CD cells were allowed to adhere for 1 h to eight-well-chamber glass slides (Millipore; Millicell EZ slides, catalog no. PEZGS0816) coated with MG (20 μ g/ml) at 4°C overnight. Adherent cells were fixed with 4% paraformaldehyde, incubated with primary antibody followed by secondary antibodies (1:100), and visualized using a Zeiss LSM 710 microscope. Images were taken close to the substrate. The intensities of images were analyzed using ImageJ software, and the 9EG7 to Ha2/5 intensity ratio was calculated.

Flow cytometry

CD cells were incubated with primary antibodies against β 1, α 1, α 2, α 3, and α 6 integrin antibodies (Table S1) followed by R-phycoerythrin-conjugated secondary antibodies (Invitrogen) diluted in FACS-TBS (30 mM Tris, pH 7.4, 180 mM NaCl, 3.5 mM KCl, supplemented with 1 mM CaCl_2 , 1 mM MgCl_2 , 3% BSA, 0.02% NaN_3) for 1 h on ice, washed twice with cold FACS-TBS, and finally incubated with the secondary antibody for 45 min on ice. For surface detection of the lipid raft marker ganglioside GM1, CD cells were incubated for 45 min on ice with FITC-conjugated cholera toxin B subunit (Sigma-Aldrich; #C1655). For surface detection of the lipid raft marker ganglioside GM1, CD cells were incubated for 45 min on ice with FITC-conjugated cholera toxin B subunit (Sigma-Aldrich; #C1655). Flow cytometry was performed with a BD LSRFortessa flow cytometer (BD Biosciences) equipped with FACS DiVa software (BD Biosciences) using standard procedures. Data analysis was performed with the FlowJo program.

Cytoskeletal fractionation

For cytoskeletal fractionation, a modified triton solubility assay was performed as previously described (Sato et al., 2017). Briefly, cells were washed with prewarmed Pipes-EGTA-magnesium (PEM) buffer (100 mM Pipes-NaOH, pH 6.8, 1 mM EGTA, and 2 mM MgCl_2) and gently permeabilized with

prewarmed PEMT buffer (0.2% Triton X-100 in PEM) at 37°C for 1 min without shaking. The permeabilized cell extract was collected into a plastic tube. More prewarmed PEM buffer was gently added to the sample on the plate, and the resulting rinsed buffer was immediately collected into the same tube. These two collections are the cytosolic fraction, which was mixed with 4X SDS sample buffer. After rinsing, the residual cells only containing the detergent resistant actin cytoskeleton were lysed with 4X SDS sample buffer and collected into a plastic tube (cytoskeletal fraction). The samples were further denatured by boiling for 5 min and then loaded for immunoblotting.

Histology and immunofluorescence

For histological and morphological analysis, kidneys were removed at different stages of development and at the indicated ages in adults and fixed in 4% formaldehyde and embedded in paraffin. Paraffin tissue sections (5 μm) were stained with hematoxylin and eosin for morphological evaluation by light microscopy. Collagen accumulation in kidney sections was determined by staining for Sirius red and quantified by image analysis. Analysis was made without knowledge of the treatment protocol. In brief, paraffin kidney sections incubated in picosirius red solution (Sigma-Aldrich) in 500 ml saturated aqueous solution of picric acid for 1 h and then washed in two changes of acidified water (5 ml acetic acid in 1 liter water). For immunofluorescence, paraffin kidney sections were subjected to heat-induced antigen retrieval in a citrate buffered solution (BioGenex; #HK086-9K). Sections were blocked and antibodies were diluted in 3% BSA, 10% normal horse serum, and 0.01% Tween in PBS. For mounting, Prolong Gold Antifade was used (Thermo Fisher; #P10144). CDs were labeled with DBA (Vector Labs; FITC conjugated, 1:100, #FL-1031) applied together with secondary antibodies. Where indicated (for E-cadherin, Ezrin, and acetylated tubulin), z-stacks with full-thickness maximum intensity projections of paraffin sections are shown. In vivo line-scan profiling of AQP2-positive CDs was performed by using ImageJ to draw a line perpendicular to the apical membrane and plotting the normalized (to negative control) intensity profile along the line axis. In vitro, immunofluorescence was performed as previously described. Images were collected with confocal microscopy (Leica TCS SPE or Zeiss LSM710, 780, or 880, objective 63 \times /1.4 NA Plan Apochromat oil). Line scans were performed using the plot profile tool of ImageJ software (plot profile). Primary antibodies used for immunofluorescence are listed in Table S1. The following secondary antibodies were used: Alexa Fluor 488 Anti-Rabbit (Thermo Fisher; #A21206), Alexa Fluor 594 Anti-Mouse (Thermo Fisher; #A11005), and Alexa Fluor 594 Anti-Rabbit (Thermo Fisher; #A11037).

Cdc42 and RhoA activity assays

Cdc42 activity was determined using the Rac1/Cdc42 Activation Assay Kit (Millipore-Sigma; #17-441) according to the manufacturer's instructions. Briefly, CD cells were plated on MG (20 $\mu\text{g}/\text{ml}$) for 1 h and then lysed by scraping in Mg^{2+} lysis buffer containing 25 mM Hepes, pH 7.5, 150 mM NaCl, 1% Igepal CA-630, 10 mM MgCl_2 , 1 mM EDTA, and 2% glycerol. After a centrifuge pulse, the supernatant was collected. Per 0.5 ml of cell

extract (containing 1mg of protein), 10 μg of cdc42 assay reagent (PAK-1 PBD, agarose beads) was added and incubated 60 min at 4°C with gentle rocking. Then, beads were centrifuged (5 s, 14,000 $\times g$, 4°C), washed three times in wash buffer, and then resuspended in 4X SDS buffer and boiled for 5 min at 95°C before immunoblotting. For RhoA activity, a similar protocol was performed, but RhoA assay reagent (Rhotekin RBD, agarose beads) was used (Millipore-Sigma; #17-294). Total and activated Cdc42 and RhoA were analyzed by immunoblotting as outlined above using Anti-RhoA or Anti-Cdc42, respectively.

Actin polymerization assay

Actin polymerization was assessed using the Actin Polymerization Biochem Kit (Cytoskeleton; #BK003) according to the manufacturer's instructions. Briefly, cellular extracts were prepared by lysis in M-PER reagent (Thermo Fisher; #78501), protein concentration was normalized using the BCA assay to achieve 7 $\mu\text{g}/\mu\text{l}$ per sample. The lysate was then dialyzed against XB Buffer (10 mM Hepes, pH 7.7, 100 mM KCl, 2 mM MgCl, 0.1 mM CaCl, 5 mM EGTA, and 1 mM DTT) for >3 h with two exchanges using a Slide-A-Lyzer Mini device with a 10,000 molecular weight cutoff (Thermo Fisher; #88401). Next, the pyrene G-actin stock was prepared according to the manufacturer's protocol and left on ice for 1 h to depolymerize oligomers that form during storage. Actin polymerization buffer containing ATP was added to the samples in a 96-well black plate, and pyrene fluorescence was recorded with excitation/emission 350/407 nm on a Spectramax iD3 (Molecular Devices). Purified Arp2/3 complex (#RP01P) and VCA domain (#VCG03) were purchased from Cytoskeleton and used at a final concentration of 10 nM and 400 nM, respectively. The actin polymerization rate was calculated during the phase of linear increase using the following formula (RFU, relative fluorescence unit):

$$\text{Polymerization rate} \left(\text{in } \frac{\text{RFU}}{\text{min}} \right) = \frac{(\text{RFU}_{\text{final}} - \text{RFU}_{\text{initial}}) \div \Delta \text{time (min)}}{\text{min}}$$

TEM

Kidneys were perfusion fixed in 2% paraformaldehyde and 2% glutaraldehyde in 0.1 M cacodylate buffer, followed by further fixation in 2.5% glutaraldehyde and dissection of the renal papillae. Samples were then postfixed in 1% tannic acid, followed by 1% OsO_4 , and en bloc stained with 1% uranyl acetate. Samples were dehydrated using a graded ethanol series and infiltrated with epon-812 using propylene oxide as the transition solvent. The resin was polymerized at 60°C for 48 h and samples sectioned at 70 nm nominal thickness. Grids were stained with 2% uranyl acetate and lead citrate. TEM imaging was performed on a Philips/FEI T-12 operating at 100 kV using a Gatan or Advanced Microscopy Techniques charge-coupled device camera.

Wounding assay

Rac1^{f/f} or Rac1^{-/-} CD cells were grown to confluence on transwell inserts consisting of polyvinylpyrrolidone-free polycarbonate filters with 0.4- μm pores (Corning; #3460). For wounding,

confluent epithelial cell sheets were scratched with a 10- μ l pipet tip. An area adjacent to the scratch was monitored using a ZOE Fluorescent Cell Imager (Bio-Rad). As soon as the area was covered with cells of comparable density between control and mutant cells, the cell sheets were fixed and rhodamine-phalloidin labeled. Treatments (CK666 or blebbistatin) were added 1 h before fixation. The scratch-adjacent areas were imaged using a confocal Olympus FV-1000 microscope with a 100 \times objective (1.40 SPlan-UApo oil), and lateral F-actin height was measured using ImageJ.

FRAP

FRAP using the cell-permeable live-imaging F-actin dye SiR-actin was performed as previously described, with some modifications (Gokhin et al., 2015). Briefly, Rac1^{f/f} or Rac1^{-/-} CD cells were plated at high density (300,000 cells/well) onto transwell inserts consisting of polycarbonate filters with 0.4 μ m pores (Corning; #3460). Cells were incubated for 6 h with Live Cell Imaging Solution (+10% FBS) from Molecular Probes (#A14291D) supplemented with 100 nM SiR-actin (Cytoskeleton; #CY-SC001) for actin labeling and 1 μ M verapamil, an efflux pump inhibitor to improve dye retention and staining. Imaging and bleaching was performed using the FRAP module of a Zeiss LSM780 confocal microscope with a 63 \times /1.40 Plan Apochromat oil objective. An $\sim 2 \times 1$ - μ m ROI at points of initial lateral cell-cell contact in early cell layers was bleached with a 561-nm laser at 100% laser power. Images were acquired at one image every 10 s for 5 min. At least 10 cell-cell contacts were analyzed per experiment. Analysis was performed with ImageJ, and GraphPad Prism was used for exponential curve fitting.

In vivo F-actin labeling

Kidneys were perfusion fixed in 2% paraformaldehyde and 2% glutaraldehyde in PBS, and the renal papillae were dissected. For cryoprotection, papillae were then incubated in 30% sucrose for 48 h, after which they were transferred into cryomolds for optimal cutting temperature compound tissue embedding. Thick cryosectioning was performed at 50 μ m thickness using a Leica cryostat. Sections were dried, rehydrated, and incubated with Alexa Fluor 647 phalloidin (Thermo Fisher; #A22287, 1:50) for 24 h. For simple immersion, aqueous-based optical clearing sections were incubated in refractive index matching solutions (40 g of Histodenz in 30 ml of 0.02 M phosphate buffer with 0.01% sodium azide, brought to a pH of 7.5 with NaOH) for 2–3 h or until sections became translucent. Confocal imaging was performed with a Zeiss LSM880 with Airy Scan.

Human samples

Formalin-fixed, paraffin-embedded tissue sections were obtained from deidentified tumor nephrectomy (renal cell cancer) specimens through the Department of Pathology at Vanderbilt University Medical Center (VUMC). Images were obtained from the nontumor healthy portion of the section. This use of human deidentified samples was approved by the VUMC institutional review board.

Statistics

Data are shown as mean \pm SD or SEM. Unpaired two-tailed *t* test was used to evaluate statistically significant differences (*, *P* <

0.05) between two groups. One-way ANOVA was used to test statistical significance (*, *P* < 0.05) among multiple groups. Post-hoc comparisons of ANOVA were corrected with the method of Tukey. For fold-change calculations (e.g., Western blot densitometry), the control number was normalized to 1 for each comparison and does not have an error bar. Data distribution was assumed to be normal, but this was not formally tested. GraphPad Prism software was used for statistical analysis.

Online supplemental material

Fig. S1 shows Rac1 immunostaining of Rac1^{f/f} and Hoxb7:Rac1^{-/-} collecting ducts of different ages. Fig. S2 shows integrin activation images corresponding to Fig. 4, Rho GTPase activities in Rac1^{f/f} vs Rac1^{-/-} CD cells, and WAVE2 and Arp2 levels in Rac1^{f/f} and Hoxb7:Rac1^{-/-} papillary lysates in vivo. Fig. S3 shows that Arp2/3 inhibition of WT CD cells mimics Rac1 deficiency. Fig. S4 shows that MLCK inhibition is insufficient to rescue the epithelial defects of Rac1^{-/-} CD cells. Fig. S5 shows that low-dose blebbistatin rescues the adhesion defect of Rac1^{-/-} CD cells and representative wounding assay images with scratch-adjacent cell density quantification corresponding to Fig. 9. Table S1 lists primary antibodies and dilutions used in this study.

Acknowledgments

This work was supported in part by U.S. Department of Veterans Affairs Merit Reviews 1I01BX002196 (R. Zent), 1I01BX002025 (A. Pozzi), and 1I01BX003425 (L.S. Gewin); and National Institutes of Health grants R01-DK069921 and R01-DK127589 (R. Zent), R01-DK119212 (A. Pozzi), R01-DK-108968-01 (L. Gewin), R01-DK56942 (A.B. Foggo), P30-DK114809 (R. Zent, A. Pozzi, L.S. Gewin, and A.B. Foggo), and 2T32DK007569-32 (F. Bock and A.S. Terker). F. Bock is the recipient of an American Society of Nephrology Ben J. Lipps Research Fellowship. A.S. Terker is the recipient of an American Heart Association postdoctoral fellowship. A. Pozzi is the recipient of a U.S. Department of Veterans Affairs Senior Research Career Scientist award. Confocal imaging, electron microscopy, and image analysis were performed in part using the Vanderbilt Cell Imaging Shared Resource (supported by National Institutes of Health grants CA68485, DK20593, DK58404, DK59637, and EY08126). The Zeiss LSM880 Airy Scan is supported by National Institutes of Health grant S10-OD021630. Flow cytometry experiments were performed in the VUMC Flow Cytometry Shared Resource. The VUMC Flow Cytometry Shared Resource is supported by the Vanderbilt-Ingram Cancer Center (P30 CA68485) and the Vanderbilt Digestive Disease Research Center (DK058404). Histology was performed with the support of the Translational Pathology Shared Resource (National Cancer Institute/National Institutes of Health Cancer Center Support Grant 5P30 CA68485-19).

The authors declare no competing financial interests.

Author contributions: F. Bock contributed to formal analysis, investigation, methodology, original draft, review, and editing; B.C. Elias, X. Dong, and D.V. Parekh contributed to investigation and methodology; G. Mernaugh and O.M. Viquez contributed to investigation and project administration; A. Hassan, V.R. Amara, J. Liu, A.S. Terker, M. Chiusa, and K.L. Brown contributed to

investigation; L.S. Gewin, A.B. Fogo, and C.H. Brakebusch contributed to resources, review, and editing; A. Pozzi contributed to funding acquisition, resources, review, and editing; and R. Zent contributed to funding acquisition, conceptualization, investigation, visualization, original draft, review, and editing.

Submitted: 2 April 2021

Revised: 27 July 2021

Accepted: 8 September 2021

References

- Abella, J.V., C. Galloni, J. Pernier, D.J. Barry, S. Kjær, M.F. Carlier, and M. Way. 2016. Isoform diversity in the Arp2/3 complex determines actin filament dynamics. *Nat. Cell Biol.* 18:76–86. <https://doi.org/10.1038/ncb3286>
- Aguilar-Aragon, M., A. Elbediwy, V. Foglizzo, G.C. Fletcher, V.S.W. Li, and B.J. Thompson. 2018. Pak1 Kinase Maintains Apical Membrane Identity in Epithelia. *Cell Rep.* 22:1639–1646. <https://doi.org/10.1016/j.celrep.2018.01.060>
- Akhtar, N., and C.H. Streuli. 2006. Rac1 links integrin-mediated adhesion to the control of lactational differentiation in mammary epithelia. *J. Cell Biol.* 173:781–793. <https://doi.org/10.1083/jcb.200601059>
- Berrier, A.L., R. Martinez, G.M. Bokoch, and S.E. LaFlamme. 2002. The integrin beta tail is required and sufficient to regulate adhesion signaling to Rac1. *J. Cell Sci.* 115:4285–4291. <https://doi.org/10.1242/jcs.00109>
- Bokoch, G.M., A.M. Reilly, R.H. Daniels, C.C. King, A. Olivera, S. Spiegel, and U.G. Knaus. 1998. A GTPase-independent mechanism of p21-activated kinase activation. Regulation by sphingosine and other biologically active lipids. *J. Biol. Chem.* 273:8137–8144. <https://doi.org/10.1074/jbc.273.14.8137>
- Bosco, E.E., J.C. Mulloy, and Y. Zheng. 2009. Rac1 GTPase: a “Rac” of all trades. *Cell. Mol. Life Sci.* 66:370–374. <https://doi.org/10.1007/s00018-008-8552-x>
- Bray, K., M. Gillette, J. Young, E. Loughran, M. Hwang, J.C. Sears, and T. Vargo-Gogola. 2013. Cdc42 overexpression induces hyperbranching in the developing mammary gland by enhancing cell migration. *Breast Cancer Res.* 15:R91. <https://doi.org/10.1186/bcr3487>
- Brieher, W.M., and A.S. Yap. 2013. Cadherin junctions and their cytoskeleton(s). *Curr. Opin. Cell Biol.* 25:39–46. <https://doi.org/10.1016/j.cob.2012.10.010>
- Cebrián, C., K. Borodo, N. Charles, and D.A. Herzlinger. 2004. Morphometric index of the developing murine kidney. *Dev. Dyn.* 231:601–608. <https://doi.org/10.1002/dvdy.20143>
- Chauhan, B.K., M. Lou, Y. Zheng, and R.A. Lang. 2011. Balanced Rac1 and RhoA activities regulate cell shape and drive invagination morphogenesis in epithelia. *Proc. Natl. Acad. Sci. USA.* 108:18289–18294. <https://doi.org/10.1073/pnas.1108993108>
- Chen, B., H.T. Chou, C.A. Brautigam, W. Xing, S. Yang, L. Henry, L.K. Doolittle, T. Walz, and M.K. Rosen. 2017. Rac1 GTPase activates the WAVE regulatory complex through two distinct binding sites. *eLife.* 6:e29795. <https://doi.org/10.7554/eLife.29795>
- Chrostek, A., X. Wu, F. Quondamatteo, R. Hu, A. Sanecka, C. Niemann, L. Langbein, I. Haase, and C. Brakebusch. 2006. Rac1 is crucial for hair follicle integrity but is not essential for maintenance of the epidermis. *Mol. Cell Biol.* 26:6957–6970. <https://doi.org/10.1128/MCB.00075-06>
- Connell, L.E., and D.M. Helfman. 2006. Myosin light chain kinase plays a role in the regulation of epithelial cell survival. *J. Cell Sci.* 119:2269–2281. <https://doi.org/10.1242/jcs.02926>
- Costantini, F., and R. Kopan. 2010. Patterning a complex organ: branching morphogenesis and nephron segmentation in kidney development. *Dev. Cell.* 18:698–712. <https://doi.org/10.1016/j.devcel.2010.04.008>
- Couto, A., N.A. Mack, L. Favia, and M. Georgiou. 2017. An apicobasal gradient of Rac activity determines protrusion form and position. *Nat. Commun.* 8:15385. <https://doi.org/10.1038/ncomms15385>
- Daneshjoui, N., N. Sieracki, G.P. van Nieuw Amerongen, D.E. Conway, M.A. Schwartz, Y.A. Komarova, and A.B. Malik. 2015. Rac1 functions as a reversible tension modulator to stabilize VE-cadherin trans-interaction. *J. Cell Biol.* 208:23–32. <https://doi.org/10.1083/jcb.201409108>
- Danopoulos, S., M. Krainock, O. Toubat, M. Thornton, B. Grubbs, and D. Al Alam. 2016. Rac1 modulates mammalian lung branching morphogenesis in part through canonical Wnt signaling. *Am. J. Physiol. Lung Cell. Mol. Physiol.* 311:L1036–L1049. <https://doi.org/10.1152/ajplung.00274.2016>
- del Pozo, M.A., N.B. Alderson, W.B. Kioussis, H.H. Chiang, R.G. Anderson, and M.A. Schwartz. 2004. Integrins regulate Rac targeting by internalization of membrane domains. *Science.* 303:839–842. <https://doi.org/10.1126/science.1092571>
- Delaney, M.K., J. Liu, Y. Zheng, M.C. Berndt, and X. Du. 2012. The role of Rac1 in glycoprotein Ib-IX-mediated signal transduction and integrin activation. *Arterioscler. Thromb. Vasc. Biol.* 32:2761–2768. <https://doi.org/10.1161/ATVBAHA.112.254920>
- deLeon, O., J.M. Puglise, F. Liu, J. Smits, M.B. ter Beest, and M.M. Zegers. 2012. Pak1 regulates the orientation of apical polarization and lumen formation by distinct pathways. *PLoS One.* 7:e41039. <https://doi.org/10.1371/journal.pone.0041039>
- Delorme, V., M. Machacek, C. DerMardirossian, K.L. Anderson, T. Wittmann, D. Hanein, C. Waterman-Storer, G. Danuser, and G.M. Bokoch. 2007. Cofilin activity downstream of Pak1 regulates cell protrusion efficiency by organizing lamellipodium and lamella actin networks. *Dev. Cell.* 13:646–662. <https://doi.org/10.1016/j.devcel.2007.08.011>
- Denker, B.M., and E. Sabath. 2011. The biology of epithelial cell tight junctions in the kidney. *J. Am. Soc. Nephrol.* 22:622–625. <https://doi.org/10.1681/ASN.2010090922>
- Dimchev, V., I. Lahmann, S.A. Koestler, F. Kage, G. Dimchev, A. Steffen, T.E.B. Stradal, F. Vauti, H.H. Arnold, and K. Rottner. 2021. Induced Arp2/3 Complex Depletion Increases FMNL2/3 Formin Expression and Filopodia Formation. *Front. Cell Dev. Biol.* 9:634708. <https://doi.org/10.3389/fcell.2021.634708>
- Doyle, A.D., N. Carvajal, A. Jin, K. Matsumoto, and K.M. Yamada. 2015. Local 3D matrix microenvironment regulates cell migration through spatio-temporal dynamics of contractility-dependent adhesions. *Nat. Commun.* 6:8720. <https://doi.org/10.1038/ncomms9720>
- Efimova, N., and T.M. Svitkina. 2018. Branched actin networks push against each other at adherens junctions to maintain cell-cell adhesion. *J. Cell Biol.* 217:1827–1845. <https://doi.org/10.1083/jcb.201708103>
- Elias, B.C., A. Das, D.V. Parekh, G. Mernaugh, R. Adams, Z. Yang, C. Brakebusch, A. Pozzi, D.K. Marciano, T.J. Carroll, et al. 2015. Cdc42 regulates epithelial cell polarity and cytoskeletal function during kidney tubule development. *J. Cell Sci.* 128:4293–4305.
- Georgiou, M., and B. Baum. 2010. Polarity proteins and Rho GTPases cooperate to spatially organise epithelial actin-based protrusions. *J. Cell Sci.* 123:1089–1098. <https://doi.org/10.1242/jcs.060772>
- Gokhin, D.S., R.B. Nowak, J.A. Khoory, A.L. Piedra, I.C. Ghiran, and V.M. Fowler. 2015. Dynamic actin filaments control the mechanical behavior of the human red blood cell membrane. *Mol. Biol. Cell.* 26:1699–1710. <https://doi.org/10.1091/mbc.E14-12-1583>
- Goley, E.D., and M.D. Welch. 2006. The ARP2/3 complex: an actin nucleator comes of age. *Nat. Rev. Mol. Cell Biol.* 7:713–726. <https://doi.org/10.1038/nrm2026>
- Goodwin, K., and C.M. Nelson. 2020. Branching morphogenesis. *Development.* 147:dev184499. <https://doi.org/10.1242/dev.184499>
- Husted, R.F., M. Hayashi, and J.B. Stokes. 1988. Characteristics of papillary collecting duct cells in primary culture. *Am. J. Physiol.* 255:F1160–F1169. <https://doi.org/10.1152/ajprenal.1988.255.6.F1160>
- Ivanov, A.I., C.A. Parkos, and A. Nusrat. 2010. Cytoskeletal regulation of epithelial barrier function during inflammation. *Am. J. Pathol.* 177:512–524. <https://doi.org/10.2353/ajpath.2010.100168>
- Ke, Y., M. Lei, X. Wang, and R.J. Solaro. 2013. Unique catalytic activities and scaffolding of p21 activated kinase-1 in cardiovascular signaling. *Front. Pharmacol.* 4:116. <https://doi.org/10.3389/fphar.2013.00116>
- Kim, M.J., J.Y. Byun, C.H. Yun, I.C. Park, K.H. Lee, and S.J. Lee. 2008. c-Src-p38 mitogen-activated protein kinase signaling is required for Akt activation in response to ionizing radiation. *Mol. Cancer Res.* 6:1872–1880. <https://doi.org/10.1158/1541-7786.MCR-08-0084>
- Koestler, S.A., A. Steffen, M. Nemethova, M. Winterhoff, N. Luo, J.M. Holleboom, J. Krupp, S. Jacob, M. Vinzenz, F. Schur, et al. 2013. Arp2/3 complex is essential for actin network treadmill as well as for targeting of capping protein and cofilin. *Mol. Biol. Cell.* 24:2861–2875. <https://doi.org/10.1091/mbc.e12-12-0857>
- Kumaran, G.K., and I. Hanukoglu. 2020. Identification and classification of epithelial cells in nephron segments by actin cytoskeleton patterns. *FEBS J.* 287:1176–1194. <https://doi.org/10.1111/febs.15088>
- Lee, N.K., K.W. Fok, A. White, N.H. Wilson, C.J. O’Leary, H.L. Cox, M. Michael, A.S. Yap, and H.M. Cooper. 2016. Neogenin recruitment of the WAVE regulatory complex maintains adherens junction stability and tension. *Nat. Commun.* 7:11082. <https://doi.org/10.1038/ncomms11082>

- Leiz, J., and K.M. Schmidt-Ott. 2019. Claudins in the Renal Collecting Duct. *Int. J. Mol. Sci.* 21:221. <https://doi.org/10.3390/ijms21010221>
- Leng, Y., J. Zhang, K. Badour, E. Arpaia, S. Freeman, P. Cheung, M. Siu, and K. Siminovitch. 2005. Abelson-interactor-1 promotes WAVE2 membrane translocation and Abelson-mediated tyrosine phosphorylation required for WAVE2 activation. *Proc. Natl. Acad. Sci. USA.* 102:1098–1103. <https://doi.org/10.1073/pnas.0409120102>
- Li, J.X.H., V.W. Tang, and W.M. Brieher. 2020. Actin protrusions push at apical junctions to maintain E-cadherin adhesion. *Proc. Natl. Acad. Sci. USA.* 117:432–438. <https://doi.org/10.1073/pnas.1908654117>
- Liu, W., M. Zi, R. Naumann, S. Ulm, J. Jin, D.M. Taglieri, S. Prehar, J. Gui, H. Tsui, R.P. Xiao, et al. 2011. Pak1 as a novel therapeutic target for anti-hypertrophic treatment in the heart. *Circulation.* 124:2702–2715. <https://doi.org/10.1161/CIRCULATIONAHA.111.048785>
- Löf-Öhlin, Z.M., P. Nyeng, M.E. Bechard, K. Hess, E. Bankaitis, T.U. Greiner, J. Ameri, C.V. Wright, and H. Semb. 2017. EGFR signalling controls cellular fate and pancreatic organogenesis by regulating apical-basal polarity. *Nat. Cell Biol.* 19:1313–1325. <https://doi.org/10.1038/ncb3628>
- Lu, Z., S. Mathew, J. Chen, A. Hadziselimovic, R. Palamuttam, B.G. Hudson, R. Fässler, A. Pozzi, C.R. Sanders, and R. Zent. 2016. Implications of the differing roles of the $\beta 1$ and $\beta 3$ transmembrane and cytoplasmic domains for integrin function. *eLife.* 5:e18633. <https://doi.org/10.7554/eLife.18633>
- Mack, N.A., and M. Georgiou. 2014. The interdependence of the Rho GTPases and apical-basal cell polarity. *Small GTPases.* 5:e973768. <https://doi.org/10.4161/21541248.2014.973768>
- Martin, E., M.H. Ouellette, and S. Jenna. 2016. Rac1/RhoA antagonism defines cell-to-cell heterogeneity during epidermal morphogenesis in nematodes. *J. Cell Biol.* 215:483–498. <https://doi.org/10.1083/jcb.201604015>
- Mendoza, M.C. 2013. Phosphoregulation of the WAVE regulatory complex and signal integration. *Semin. Cell Dev. Biol.* 24:272–279. <https://doi.org/10.1016/j.semcdb.2013.01.007>
- Morrison, M.M., C.D. Young, S. Wang, T. Sobolik, V.M. Sanchez, D.J. Hicks, R.S. Cook, and D.M. Brantley-Sieders. 2015. mTOR Directs Breast Morphogenesis through the PKC- α -Rac1 Signaling Axis. *PLoS Genet.* 11:e1005291. <https://doi.org/10.1371/journal.pgen.1005291>
- Morrissey, M.A., and D.R. Sherwood. 2015. An active role for basement membrane assembly and modification in tissue sculpting. *J. Cell Sci.* 128:1661–1668. <https://doi.org/10.1242/jcs.168021>
- Nedeva, I., G. Koripelly, D. Caballero, L. Chièze, B. Guichard, B. Romain, E. Pencreach, J.M. Lehn, M.F. Carlier, and D. Riveline. 2013. Synthetic polyamines promote rapid lamellipodial growth by regulating actin dynamics. *Nat. Commun.* 4:2165. <https://doi.org/10.1038/ncomms3165>
- O'Brien, L.E., T.S. Jou, A.L. Pollack, Q. Zhang, S.H. Hansen, P. Yurchenco, and K.E. Mostov. 2001. Rac1 orientates epithelial apical polarity through effects on basolateral laminin assembly. *Nat. Cell Biol.* 3:831–838. <https://doi.org/10.1038/ncb0901-831>
- Otani, T., T.P. Nguyen, S. Tokuda, K. Sugihara, T. Sugawara, K. Furuse, T. Miura, K. Ebnet, and M. Furuse. 2019. Claudins and JAM-A coordinately regulate tight junction formation and epithelial polarity. *J. Cell Biol.* 218:3372–3396. <https://doi.org/10.1083/jcb.201812157>
- Pearce, D., R. Soundararajan, C. Trimpert, O.B. Kashlan, P.M. Deen, and D.E. Kohan. 2015. Collecting duct principal cell transport processes and their regulation. *Clin. J. Am. Soc. Nephrol.* 10:135–146. <https://doi.org/10.2215/CJN.05760513>
- Pichaud, F., R.F. Walther, and F. Nunes de Almeida. 2019. Regulation of Cdc42 and its effectors in epithelial morphogenesis. *J. Cell Sci.* 132:jcs217869. <https://doi.org/10.1242/jcs.217869>
- Pizarro-Cerdá, J., D.S. Chores, B. Geiger, and P. Cossart. 2017. The Diverse Family of Arp2/3 Complexes. *Trends Cell Biol.* 27:93–100. <https://doi.org/10.1016/j.tcb.2016.08.001>
- Qiao, J., R. Uzzo, T. Obara-Ishihara, L. Degenstein, E. Fuchs, and D. Herzlinger. 1999. FGF-7 modulates ureteric bud growth and nephron number in the developing kidney. *Development.* 126:547–554. <https://doi.org/10.1242/dev.126.3.547>
- Quiros, M., and A. Nusrat. 2014. RhoGTPases, actomyosin signaling and regulation of the epithelial Apical Junctional Complex. *Semin. Cell Dev. Biol.* 36:194–203. <https://doi.org/10.1016/j.semcdb.2014.09.003>
- Rauscher, A.A., M. Gyimesi, M. Kovács, and A. Málnási-Csizmadia. 2018. Targeting Myosin by Blebbistatin Derivatives: Optimization and Pharmacological Potential. *Trends Biochem. Sci.* 43:700–713. <https://doi.org/10.1016/j.tibs.2018.06.006>
- Reymann, A.C., R. Boujemaa-Paterski, J.L. Martiel, C. Guérin, W. Cao, H.F. Chin, E.M. De La Cruz, M. Théry, and L. Blanchoin. 2012. Actin network architecture can determine myosin motor activity. *Science.* 336:1310–1314. <https://doi.org/10.1126/science.1221708>
- Riveline, D., R. Thiagarajan, J.M. Lehn, and M.F. Carlier. 2014. Synthetic polyamines: new compounds specific to actin dynamics for mammalian cell and fission yeast. *Bioarchitecture.* 4:144–148. <https://doi.org/10.4161/19490992.2014.965111>
- Rodgers, L.S., and A.S. Fanning. 2011. Regulation of epithelial permeability by the actin cytoskeleton. *Cytoskeleton (Hoboken).* 68:653–660. <https://doi.org/10.1002/cm.20547>
- Salomon, J., C. Gaston, J. Magescas, B. Duvauchelle, D. Canioni, L. Sengmanivong, A. Mayeux, G. Michaux, F. Campeotto, J. Lemale, et al. 2017. Contractile forces at tricellular contacts modulate epithelial organization and monolayer integrity. *Nat. Commun.* 8:13998. <https://doi.org/10.1038/ncomms13998>
- Sato, Y., Y. Murakami, and M. Takahashi. 2017. Semi-retentive cytoskeletal fractionation (SERCYF): A novel method for the biochemical analysis of the organization of microtubule and actin cytoskeleton networks. *Biochem. Biophys. Res. Commun.* 488:614–620. <https://doi.org/10.1016/j.bbrc.2017.05.083>
- Schell, C., B. Sabass, M. Helmstaedt, F. Geist, A. Abed, M. Yasuda-Yamahara, A. Sigle, J.I. Maier, F. Grahmmer, F. Siegerist, et al. 2018. ARP3 Controls the Podocyte Architecture at the Kidney Filtration Barrier. *Dev. Cell.* 47:741–757.e8. <https://doi.org/10.1016/j.devcel.2018.11.011>
- Steffen, A., M. Ladwein, G.A. Dimchev, A. Hein, L. Schwenkmezger, S. Arens, K.I. Ladwein, J. Margit Holleboom, F. Schur, J. Victor Small, et al. 2013. Rac function is crucial for cell migration but is not required for spreading and focal adhesion formation. *J. Cell Sci.* 126:4572–4588. <https://doi.org/10.1242/jcs.118232>
- Swaney, K.F., and R. Li. 2016. Function and regulation of the Arp2/3 complex during cell migration in diverse environments. *Curr. Opin. Cell Biol.* 42:63–72. <https://doi.org/10.1016/j.ceb.2016.04.005>
- Symons, M. 2011. Rac1 activation comes full circle. *EMBO J.* 30:3875–3877. <https://doi.org/10.1038/emboj.2011.330>
- Tan, W., T.R. Palmby, J. Gavard, P. Amornphimoltham, Y. Zheng, and J.S. Gutkind. 2008. An essential role for Rac1 in endothelial cell function and vascular development. *FASEB J.* 22:1829–1838. <https://doi.org/10.1096/fj.07-096438>
- Tang, V. 2017. Cell-cell adhesion interface: rise of the lateral membrane. *Fl000 Res.* 6:276. <https://doi.org/10.12688/fl000research.10680.1>
- Tu, Z., Q. Wang, T. Cui, J. Wang, H. Ran, H. Bao, J. Lu, B. Wang, J.P. Lydon, F. DeMayo, et al. 2016. Uterine Rac1 via Pak1-ERM signaling directs normal luminal epithelial integrity conducive to on-time embryo implantation in mice. *Cell Death Differ.* 23:169–181. <https://doi.org/10.1038/cdd.2015.98>
- Tushir, J.S., and C. D'Souza-Schorey. 2007. ARF6-dependent activation of ERK and Rac1 modulates epithelial tubule development. *EMBO J.* 26:1806–1819. <https://doi.org/10.1038/sj.emboj.7601644>
- Verma, S., S.P. Han, M. Michael, G.A. Gomez, Z. Yang, R.D. Teasdale, A. Raheesh, E.M. Kovacs, R.G. Ali, and A.S. Yap. 2012. A WAVE2-Arp2/3 actin nucleator apparatus supports junctional tension at the epithelial zonula adherens. *Mol. Biol. Cell.* 23:4601–4610. <https://doi.org/10.1091/mbc.e12-08-0574>
- Wan, H., C. Liu, S.E. Wert, W. Xu, Y. Liao, Y. Zheng, and J.A. Whitsett. 2013. CDC42 is required for structural patterning of the lung during development. *Dev. Biol.* 374:46–57. <https://doi.org/10.1016/j.ydbio.2012.11.030>
- Wang, Z., E. Pedersen, A. Basse, T. Lefever, K. Peyrollier, S. Kapoor, Q. Mei, R. Karlsson, A. Chrostek-Grashoff, and C. Brakebusch. 2010. Rac1 is crucial for Ras-dependent skin tumor formation by controlling Pak1-Mek-Erk hyperactivation and hyperproliferation in vivo. *Oncogene.* 29:3362–3373. <https://doi.org/10.1038/onc.2010.95>
- Weaver, A.M., M.E. Young, W.L. Lee, and J.A. Cooper. 2003. Integration of signals to the Arp2/3 complex. *Curr. Opin. Cell Biol.* 15:23–30. [https://doi.org/10.1016/S0955-0674\(02\)00015-7](https://doi.org/10.1016/S0955-0674(02)00015-7)
- Xiong, Y., C. Wang, L. Shi, L. Wang, Z. Zhou, D. Chen, J. Wang, and H. Guo. 2017. Myosin Light Chain Kinase: A Potential Target for Treatment of Inflammatory Diseases. *Front. Pharmacol.* 8:292. <https://doi.org/10.3389/fphar.2017.00292>
- Yagi, S., M. Matsuda, and E. Kiyokawa. 2012. Suppression of Rac1 activity at the apical membrane of MDCK cells is essential for cyst structure maintenance. *EMBO Rep.* 13:237–243. <https://doi.org/10.1038/embor.2011.249>
- Yang, Q., X.F. Zhang, T.D. Pollard, and P. Forscher. 2012. Arp2/3 complex-dependent actin networks constrain myosin II function in driving retrograde actin flow. *J. Cell Biol.* 197:939–956. <https://doi.org/10.1083/jcb.201111052>
- Yazlovitskaya, E.M., H.Y. Tseng, O. Viquez, T. Tu, G. Mernaugh, K.K. McKee, K. Riggins, V. Quaranta, A. Pathak, B.D. Carter, et al. 2015. Integrin $\alpha 3 \beta 1$

- regulates kidney collecting duct development via TRAF6-dependent K63-linked polyubiquitination of Akt. *Mol. Biol. Cell.* 26:1857–1874. <https://doi.org/10.1091/mbc.E14-07-1203>
- Yu, W., A. Datta, P. Leroy, L.E. O'Brien, G. Mak, T.S. Jou, K.S. Matlin, K.E. Mostov, and M.M. Zegers. 2005. Beta1-integrin orients epithelial polarity via Rac1 and laminin. *Mol. Biol. Cell.* 16:433–445. <https://doi.org/10.1091/mbc.e04-05-0435>
- Yu, W., A.M. Shewan, P. Brakeman, D.J. Eastburn, A. Datta, D.M. Bryant, Q.W. Fan, W.A. Weiss, M.M. Zegers, and K.E. Mostov. 2008. Involvement of RhoA, ROCK I and myosin II in inverted orientation of epithelial polarity. *EMBO Rep.* 9:923–929. <https://doi.org/10.1038/embor.2008.135>
- Yu, J., T.J. Carroll, J. Rajagopal, A. Kobayashi, Q. Ren, and A.P. McMahon. 2009. A Wnt7b-dependent pathway regulates the orientation of epithelial cell division and establishes the cortico-medullary axis of the mammalian kidney. *Development.* 136:161–171. <https://doi.org/10.1242/dev.022087>
- Zaidel-Bar, R., G. Zhenhuan, and C. Luxenburg. 2015. The contractome—a systems view of actomyosin contractility in non-muscle cells. *J. Cell Sci.* 128:2209–2217. <https://doi.org/10.1242/jcs.170068>
- Zhou, K., A. Muroyama, J. Underwood, R. Lylek, S. Ray, S.H. Soderling, and T. Lechler. 2013. Actin-related protein2/3 complex regulates tight junctions and terminal differentiation to promote epidermal barrier formation. *Proc. Natl. Acad. Sci. USA.* 110:E3820–E3829. <https://doi.org/10.1073/pnas.1308419110>
- Zhu, W., and C.M. Nelson. 2013. PI3K regulates branch initiation and extension of cultured mammary epithelia via Akt and Rac1 respectively. *Dev. Biol.* 379:235–245. <https://doi.org/10.1016/j.ydbio.2013.04.029>

Supplemental material

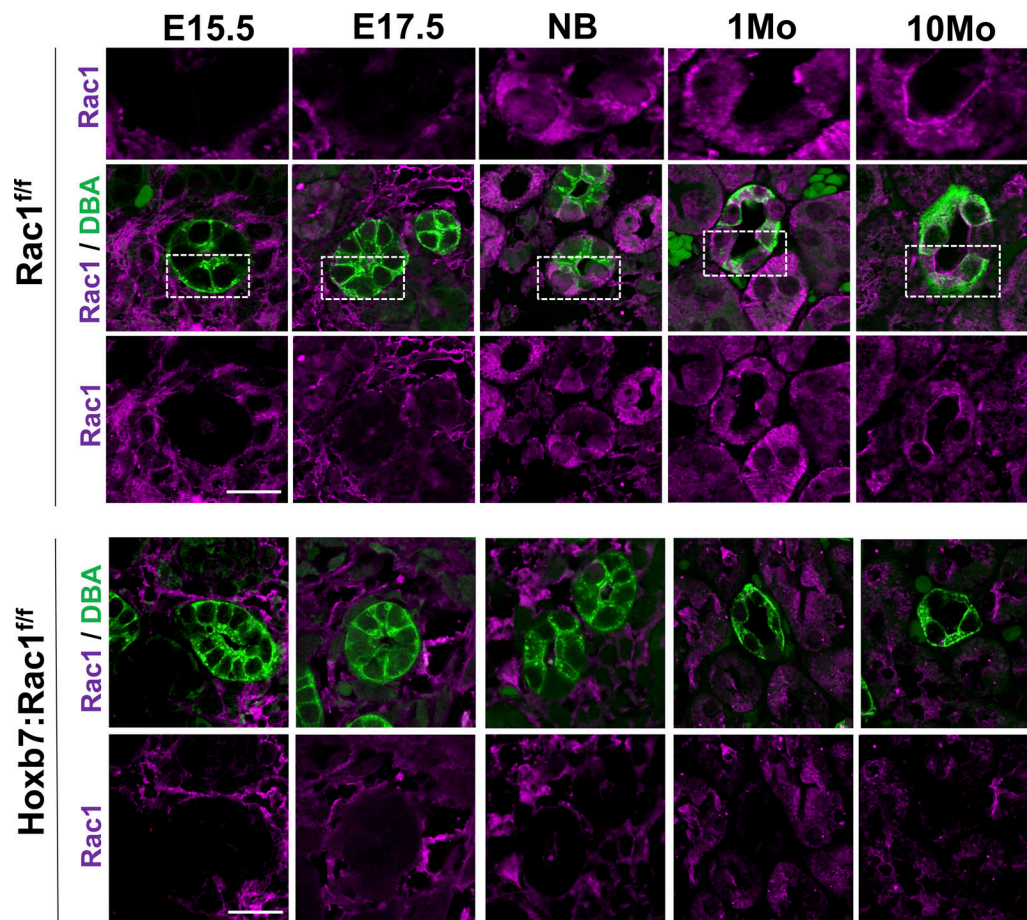


Figure S1. **Spatiotemporal assessment of Rac1 protein levels in control CDs.** (A and B) Rac1 immunostaining (magenta) was performed on control (Rac1^{f/f}; A) and Hoxb7:Rac1^{f/f} (B) paraffin kidney sections of different ages and the UB/CD labeled with DBA (green). *n* = 3 mice per group. Scale bar represents 20 μm.

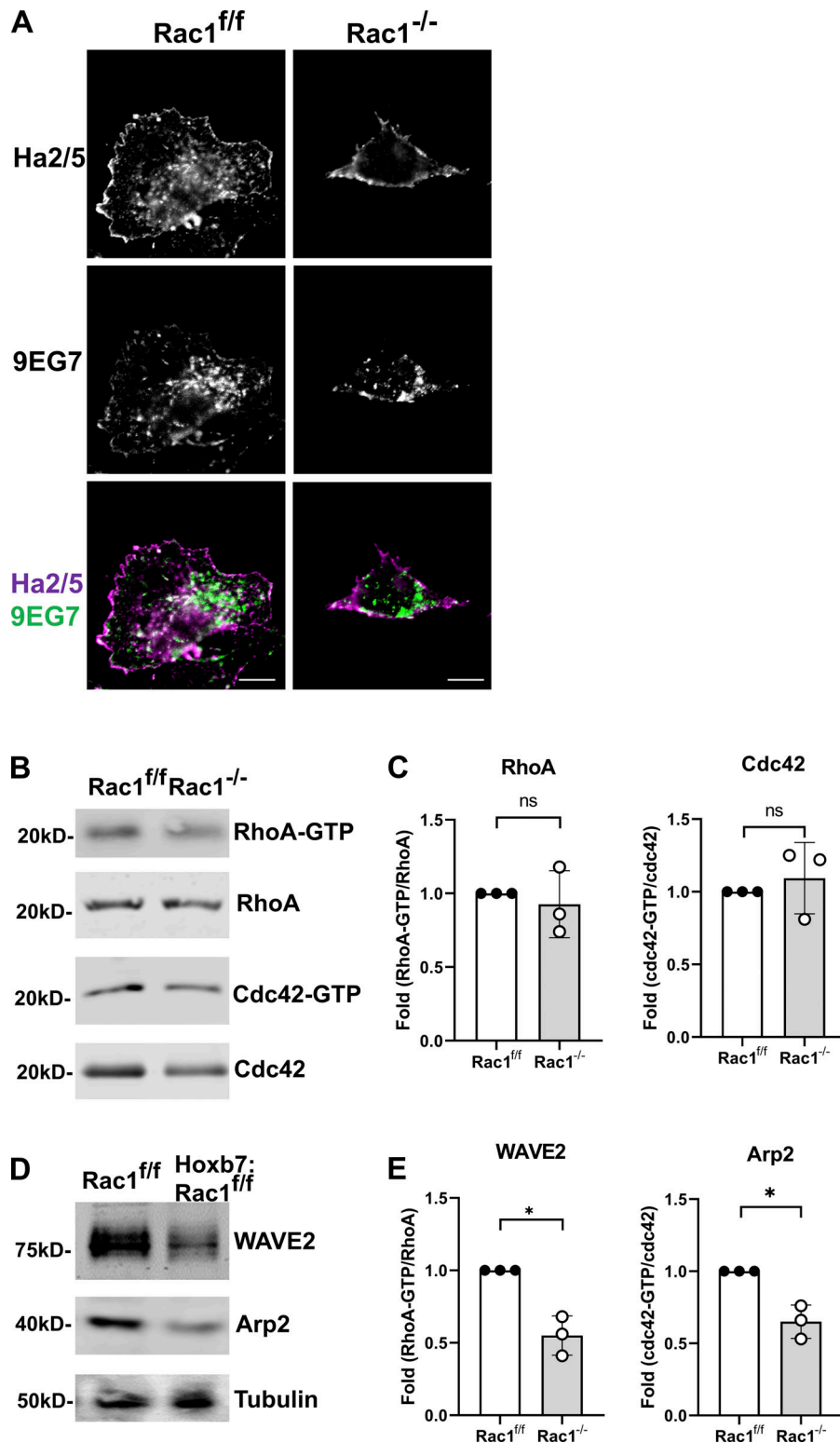


Figure S2. **Integrin activation, Rho GTPase activities in Rac1^{-/-} CD cells and WAVE2/Arp2 levels in Rac1 deficient CDs in vivo.** (A) CD cells were allowed to spread on MG for 1 h, after which they were stained for activated (9EG7) or total (Ha2/5) β 1 integrin and analyzed by laser scanning confocal microscopy. Representative images taken close to the substrate are shown. (C and D) CD cells were replated on MG and lysed after 45 min, and activated RhoA or activated Cdc42 was evaluated by pull-down assays (see Materials and methods). Activated and total RhoA and Cdc42 were analyzed by immunoblotting (A), and the ratio was calculated using densitometry in ImageJ (B). β -Actin was used to verify loading. Three experiments were performed (mean \pm SD). (D and E) Rac1^{f/f} and Hoxb7:Rac1^{f/f} papillary lysates (20 μ g/lane) were subjected to immunoblotting of WAVE2 and Arp2 (a core component of the Arp2/3 complex). A representative immunoblot is shown in D, and densitometric quantification using ImageJ of three mice per group is shown in E (mean \pm SD). β -Tubulin was used to verify loading. Scale bar represents 10 μ m (A). *, P < 0.05.

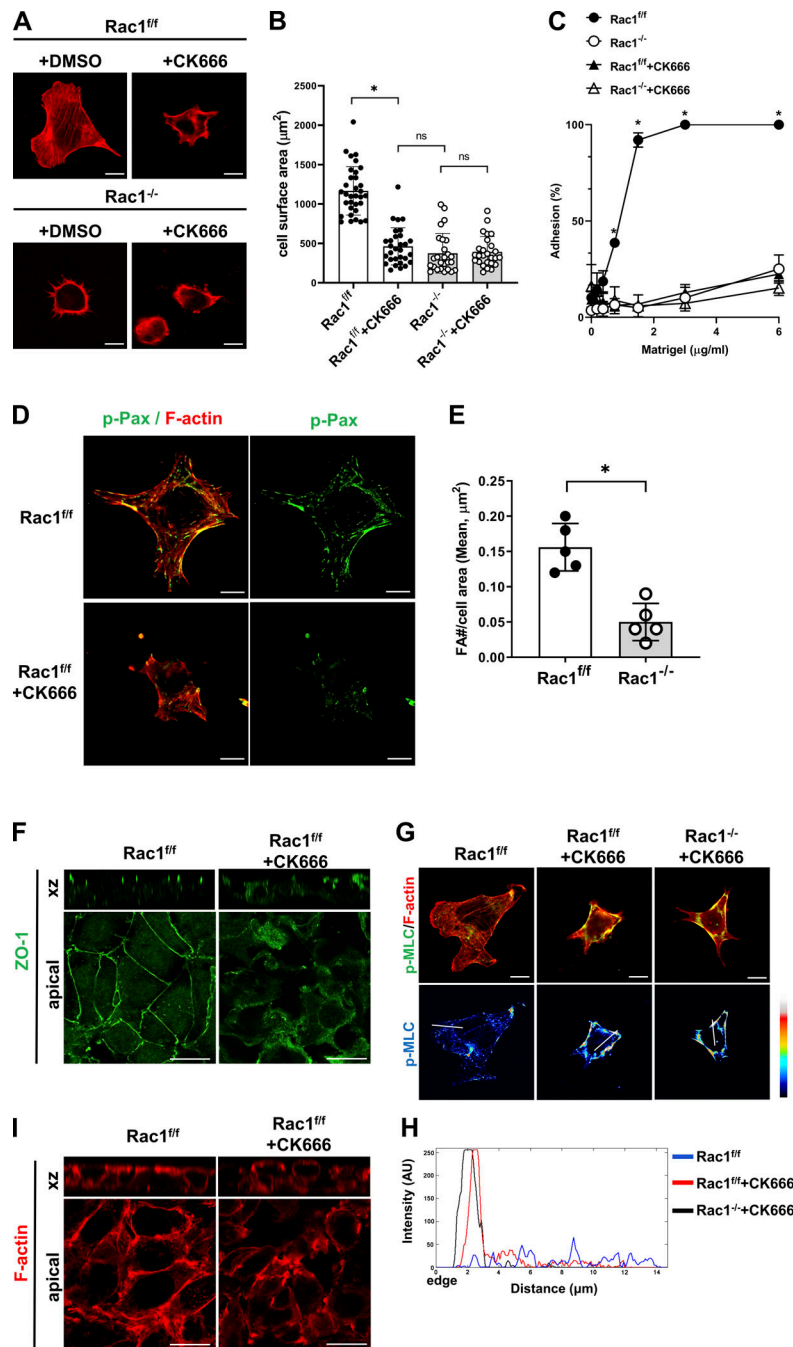


Figure S3. **Arp2/3 inhibition in WT CD cells mimics Rac1 deficiency. (A and B)** CD cells were treated with either DMSO or the Arp2/3 inhibitor CK666 (100 μM) and allowed to spread for 1 h on MG, after which they were fixed and labeled with rhodamine-phalloidin (red). Representative images are shown in A, and spreading area was quantified (B) using ImageJ/Fiji (10 cells/experiment, mean \pm SD, 20–30 cells shown as individual values). **(C)** CD cells treated with either DMSO or the Arp2/3 inhibitor CK666 (100 μM) were allowed to adhere to different concentrations of MG. Cell adhesion was evaluated 1 h after plating. Values are mean \pm SEM of three experiments. **(D and E)** $\text{Rac1}^{\text{fl/fl}}$ CD cells treated with CK666 (100 μM) were allowed to spread on MG (1 h), and focal adhesion number (phospho-paxillin, green) per cell area was analyzed in rhodamine-phalloidin (red)-labeled cells using confocal laser scanning microscopy (projection of full-thickness z-stacks) and quantified using ImageJ. Representative images are shown in D, and the mean \pm SD is shown in E. **(F)** $\text{Rac1}^{\text{fl/fl}}$ CD cells, either untreated or treated with CK666 (100 μM), were grown to confluence on transwell inserts to induce polarization and stained for ZO-1 to assess apicobasal polarization. Immunofluorescence was analyzed using confocal laser scanning microscopy with z-stacking (a minimum of 10 stacks per image). Representative images are shown. The top panels show z-stacks in xz dimension, and the bottom panels show apical cross sections. **(G and H)** $\text{Rac1}^{\text{fl/fl}}$ cells, either untreated or treated with CK666 (100 μM) and $\text{Rac1}^{-/-}$ CD cells were allowed to spread on MG for 1 h and immunostained for p-MLC (green) and costained with rhodamine-phalloidin (red; G). Line-scan analysis was performed as indicated by the white line in the bottom panels using the ImageJ/Fiji plot profile function, and a representative profile (10 cells/experiment) is shown in H. **(I)** $\text{Rac1}^{\text{fl/fl}}$ cells, either untreated or treated with CK666 (100 μM), were grown to confluence on transwell inserts to induce polarization, and F-actin was labeled with rhodamine-phalloidin (red) and analyzed using confocal laser scanning microscopy with z-stacking. Representative images in xz dimension and apical cross sections are shown. A minimum of three experiments were performed throughout. Scale bars represent 10 μm (A, D, F, G, and I). *, $P < 0.05$.

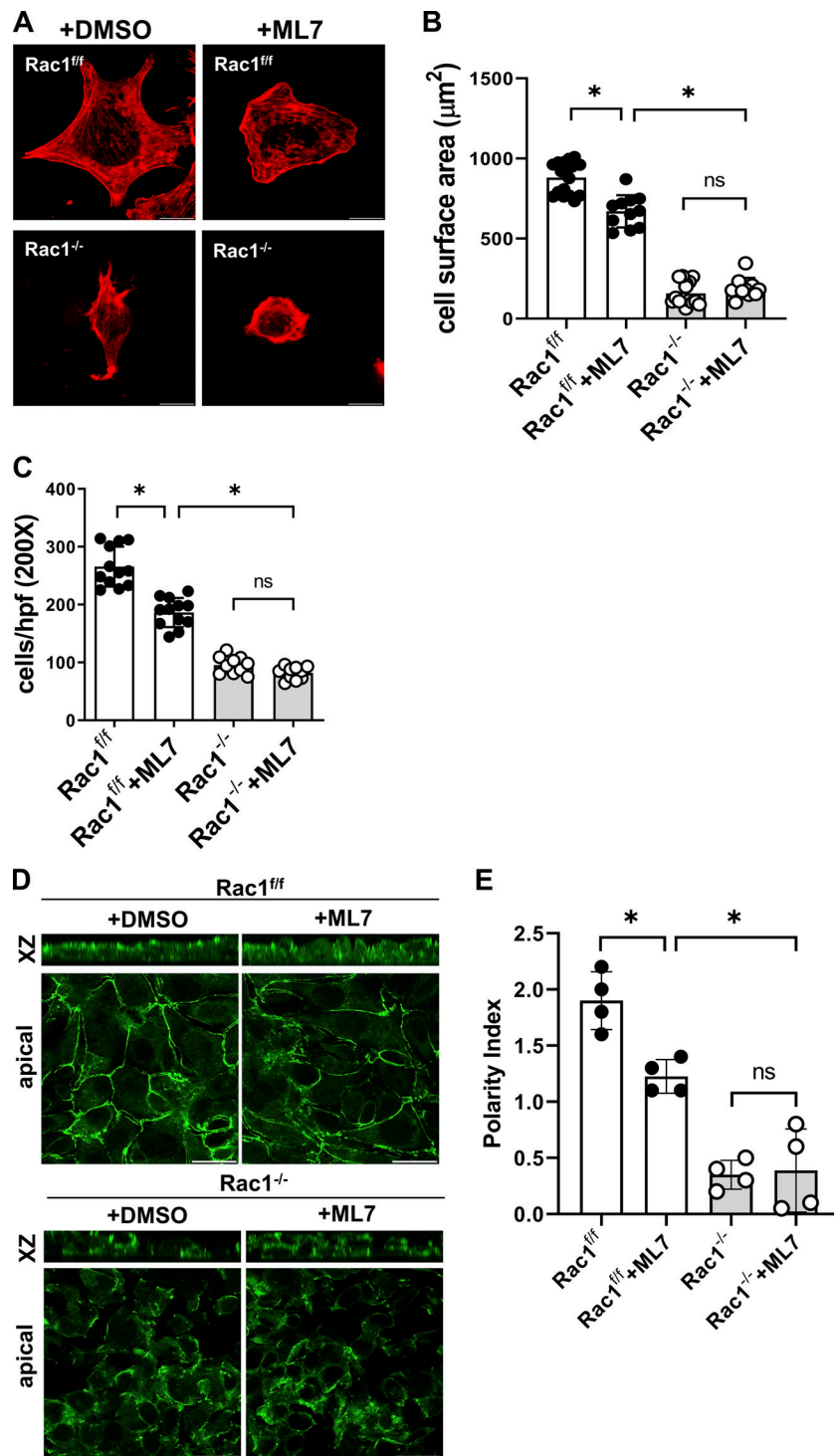


Figure S4. **MLCK inhibition does not rescue the Rac1 deficiency-induced epithelial defects.** (A and B) CD cells were treated with either DMSO or the MLCK inhibitor ML-7 (50 μM) and allowed to spread for 1 h on MG, after which they were fixed and labeled with rhodamine-phalloidin (red). Representative images are shown in A, and spreading area was quantified (B) using ImageJ/Fiji (mean \pm SD). (C) Untreated (DMSO) and ML-7-treated CD cells were plated on transwells coated with MG, and migration of DAPI-positive cells was evaluated after 4 h using the particle analyzer function in ImageJ (mean \pm SD). Scatter plots indicate individual values for at least 10 cells (B) or at least 10 fields (C). Three experiments were performed (mean \pm SD). (D and E) Untreated (DMSO) and ML-7-treated CD cells were grown to confluence on transwell inserts to induce polarization, stained for ZO-1 (green) to assess apicobasal polarization, and analyzed by confocal laser scanning microscopy. Representative images in xz dimension and apical cross sections are shown in D, and the polarization index was quantified in E (mean \pm SD, four fields). A minimum of three experiments were performed throughout. Scale bars represent 10 μm (A) and 15 μm (D). *, $P < 0.05$.

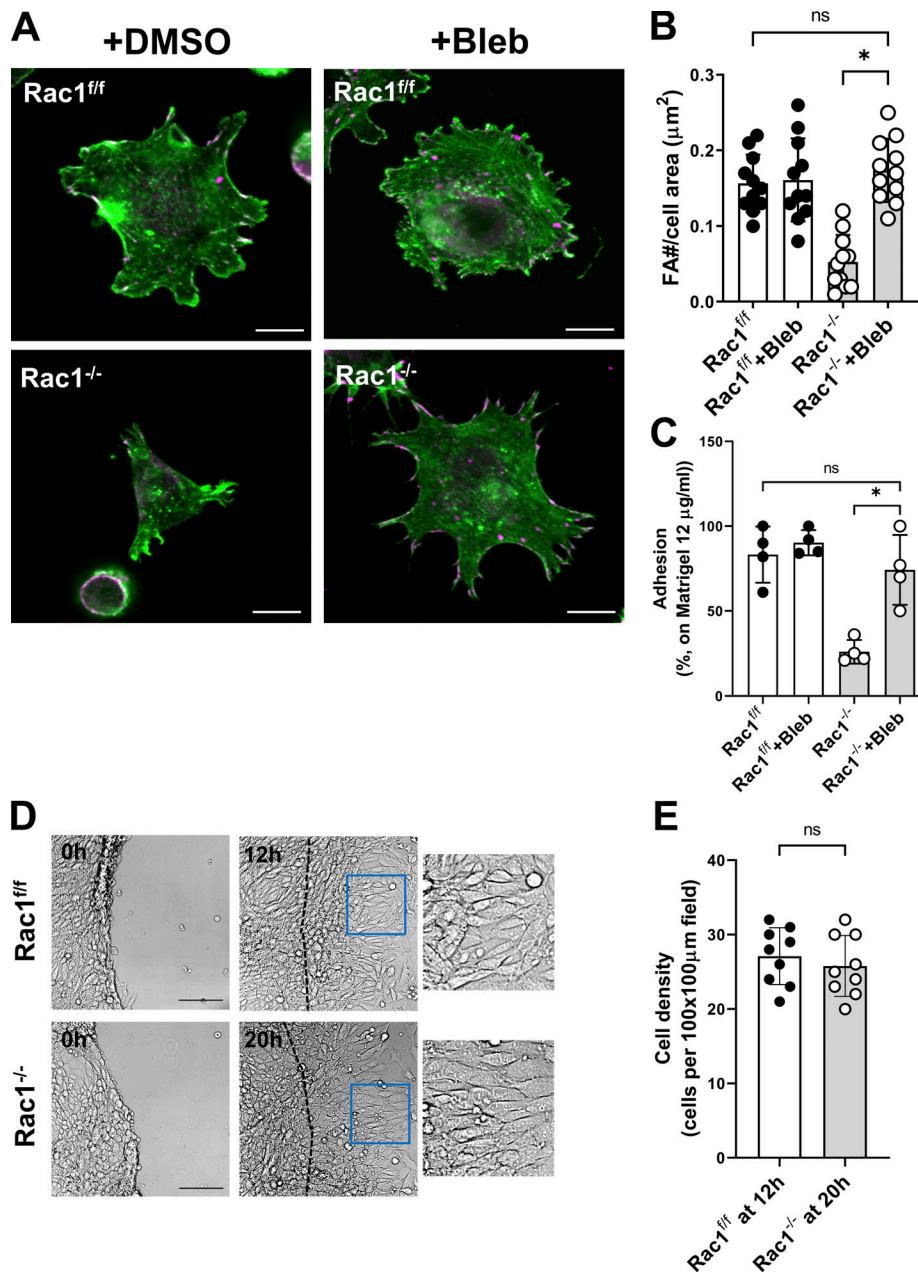


Figure S5. **Direct myosin II inhibition reverses the adhesion defect of Rac1-deficient CD cells.** (A and B) CD cells were treated either with DMSO or the myosin inhibitor blebbistatin (Bleb; 5 μ M) and allowed to spread for 1 h on MG, after which they were immunostained for the focal adhesion (FA) marker phospho-paxillin (magenta) and labeled with rhodamine-phalloidin (converted to green). Focal adhesion number per cell area was analyzed in using confocal laser scanning microscopy (projection of full-thickness z-stacks) and quantified using ImageJ. Representative images are shown in A, and the mean \pm SD of at least 10 individual cells are shown in B. (C) Blebbistatin (5 μ M)-treated CD cells were allowed to adhere to MG for 1 h, and adhesion was quantified as described in Materials and methods. Values are mean \pm SD of at least 10 individual cells. (D and E) Control images corresponding to Fig. 9 K. Confluent Rac1^{f/f} and Rac1^{-/-} CD cells were wounded and allowed to migrate until cells had covered the highlighted scratch-adjacent areas (D). Cell density was quantified and shown as scatter plots with a minimum of nine quantified fields (E). A minimum of three experiments were performed throughout. Scale bars represent 10 μ m (A) and 100 μ m (D). *, P < 0.05.

Table S1 is provided online as a separate Word file and lists the primary antibodies used in this study.